2014

Load Transfer in an Isolated Particle Embedded within an Epoxy Matrix

Erik Durnberg
University of Central Florida

STARS Citation

Durnberg, Erik, "Load Transfer in an Isolated Particle Embedded within an Epoxy Matrix" (2014). *Electronic Theses and Dissertations, 2004-2019*. 4754.
https://stars.library.ucf.edu/etd/4754

LOAD TRANSFER IN AN ISOLATED PARTICLE EMBEDDED WITHIN AN EPOXY MATRIX

by

ERIK B. DURNBERG
B.S. University of Central Florida, 2013

A thesis submitted in partial fulfillment of the requirements
for the degree of Master of Science
in the Department of Mechanical and Aerospace Engineering
in the College of Engineering and Computer Science
at the University of Central Florida
Orlando, Florida

Summer Term
2014

Major Professor:
Seetha Raghavan

Abstract

Particulate composites are widely used in many aerospace applications such as protective coatings, adhesives, or structural members of a body and their mechanical properties and behavior have gained increasing significance. The addition of modifiers such as alumina generally leads to improved mechanical properties. This addition also enables the non-invasive study of the load transfer between the particle and the matrix. Understanding the load transfer between the particulate and the matrix material is the first step to understanding the behavior and mechanical properties of the composite as a whole. In this work, samples with an isolated alumina particle embedded in an epoxy matrix were created to replicate the ideal assumptions for many particulate mechanics models. In separate experiments, both photo stimulated luminescent spectroscopy (PSLS) and synchrotron radiation were used to collect the spectral emission and diffraction rings, respectively, from the mechanically loaded samples. The PSLS data and XRD data are shown to be in qualitative agreement that as particle size is increased, the load transferred to the particle also increased for the range of particle sizes tested. This trend of increasing load transfer with increasing particle size is compared with the classical Eshelby model. Results from this work provide experimental insight into the load transfer properties of particulate composites and can serve to experimentally validate the theoretical load transfer models that currently exist.

This work is dedicated to family and friends. Their continued support and encouragement is what fueled my persistent academic efforts.

ACKNOWLEDGMENTS

First, I would like to thank my friends and family for their support and my advisor Dr. Seetha Raghavan for her guidance with my thesis along with her mentorship throughout my academic career at UCF. I would also like to thank all the members of my research team, specifically, Gregory Freihofer, Imad Hanhan and Kevin Knipe who helped me with many different aspects of this work.

This material is based upon work supported by the National Science Foundation under Grant No 1130837. In addition, some of the research described in this paper was performed at the Canadian Light Source, which is funded by the Canada Foundation for Innovation, the Natural Sciences and Engineering Research Council of Canada, the National Research Council Canada, the Canadian Institutes of Health Research, the Government of Saskatchewan, Western Economic Diversification Canada, and the University of Saskatchewan.

TABLE OF CONTENTS

LIST OF FIGURES ix

LIST OF TABLES xii

CHAPTER 1 INTRODUCTION 1

1.1 Motivation and Background 2

1.1.1 Simulations 3

1.1.2 Theoretical Models 4

1.1.3 Experiments 5

1.1.4 Alumina Particulate Composites 7

1.2 Overview of Research 8

CHAPTER 2 METHODS: PIEZOSPECTROSCOPY, THEORETICAL MODELS AND X-RAY DIFFRACTION 11

2.1 Piezospectroscopy 11

2.2 Theoretical Models 14

2.3 X-Ray Diffraction 16

CHAPTER 3 SAMPLE MANUFACTURING, AND EXPERIMENTAL SETUP 19

3.1 Sample Geometry and Manufacturing 19

  3.1.1 Alumina Particles 20

  3.1.2 Particle Size 20

  3.1.3 Irregular Shape 22

  3.1.4 Method for Suspending Particle in Matrix 23

  3.1.5 Final Samples 24

3.2 Experimental Setup 27

  3.2.1 Photo-Stimulated Luminescent Spectroscopy 27

  3.2.2 X-Ray Diffraction 31

CHAPTER 4 PIEZOSPECTROSCOPIC ANALYSIS OF ALUMINA-EPOXY SAMPLES 36

4.1 Particle Size Studies 36

  4.1.1 Small Particle Size Results 37

  4.1.2 Medium Particle Size Results 40

  4.1.3 Large Particle Size Results 42

  4.1.4 Summary of Particle Size Results 45

  4.1.5 Discussion 46

4.2 Irregular Shape 49

4.3 Failure Mechanics Using Piezospectroscopy 51

CHAPTER 5 X-RAY DIFFRACTION ANALYSIS OF ALUMINA-EPOXY SAMPLES 54

5.1 Diffraction Patterns at CLS 54

5.2 Radius Change Results 59

5.3 Strain Results 64

5.4 Conclusions 72

CHAPTER 6 CONCLUSIONS 73

LIST OF REFERENCES 76

LIST OF FIGURES

1.1 The Representative Volume Element (B) of a nanocomposite (A) 3

2.1 R1 and R2 peaks for α-Alumina 12

2.2 A spectral peak shift with applied load (A) and a peak shift versus stress plot (B) 13

3.1 A) Spherical millimeter alumina particles and B) non-spherical alumina nanoparticles 21

3.2 Images of the irregularly shaped particle under 10x magnification 23

3.3 5-step manufacturing process showing 1) mold filled half-way with epoxy, 2) placement of a single alumina particle, 3) mold filled entirely with epoxy, 4) fully cured sample, and 5) final sample extracted from mold 24

3.4 The portable spectroscopy system 28

3.5 Portable spectroscopy system schematic 29

3.6 Deconvolution and fitting of the two peaks (A) and PS coefficient determination (B) 30

3.7 PSLS experimental setup and data analysis including A) loading the samples via a mechanical load frame, B) peak determination using a least squares fit of the raw data and C) plotting of the peak shift data for a sample until failure 31

3.8 Miniature mechanical load frame used at the Canadian Light Source . . . 32

3.9 Through transmission X-ray diffraction 33

3.10 In-situ data collection using X-ray diffraction and the miniature load frame at the VESPERS beamline 34

4.1 Sample 10 R1 and R2 Peak Shift versus Stress 38

4.2 Sample 11 R1 and R2 Peak Shift versus Stress 38

4.3 Sample 12 R1 and R2 Peak Shift versus Stress 39

4.4 Sample 13 R1 and R2 Peak Shift versus Stress 40

4.5 Sample 14 R1 and R2 Peak Shift versus Stress 41

4.6 Sample 15 R1 and R2 Peak Shift versus Stress 41

4.7 Sample 16 R1 and R2 Peak Shift versus Stress 43

4.8 Sample 17 R1 and R2 Peak Shift versus Stress 43

4.9 Sample 18 R1 and R2 Peak Shift versus Stress 44

4.10 Applied uniaxial compressive stress (left) and the magnitude of the R1 peak shift (right) plotted versus time 52

5.1 Particle scan points 56

5.2 Example of a diffraction pattern collected from one of the isolated alumina particle samples 57

5.3 Changes in the diffraction pattern at different locations 58

5.4 Average radius change in the (104) peak (A) and the (113) peak (B) plotted versus applied compressive load 64

5.5 Comparison between the uncorrected (A) and corrected (B) (113) peak strains for Sample 12 66

5.6 Strain from the (113) peak for Sample 10 67

5.7 Strain from the (113) peak for Sample 12 67

5.8 Strain from the (113) peak for Sample 14 68

5.9 Strain from the (113) peak for Sample 15 68

5.10 Strain from the (113) peak for Sample 16 69

5.11 Strain from the (113) peak for Sample 18 69

5.12 Particle size effect of strain using the (113) peak 71

LIST OF TABLES

3.1 List of Samples 26

3.2 Beam, Detector and Calibration Parameters 35

4.1 Summary of Samples 37

4.2 R1 and R2 PS Coefficients (Small Samples) 39

4.3 R1 and R2 PS Coefficients (Medium Samples) 42

4.4 R1 and R2 PS Coefficients (Large Samples) 44

4.5 Particle size results including the R1 PS coefficient and hydrostatic stress ratio 46

4.6 Material Properties 47

4.7 Irregularly Shaped Particle Sample Results 50

5.1 List of XRD Samples 55

5.2 Small: Average radius change of the (104) peak with applied load 60

5.3 Medium: Average radius change of the (104) peak with applied load . . . 60

5.4 Large: Average radius change of the (104) peak with applied load 61

5.5 Small: Average radius change of the (113) peak with applied load 61

5.6 Medium: Average radius change of the (113) peak with applied load . . . 62

5.7 Large: Average radius change of the (113) peak with applied load 62

5.8 Beam, Detector and Calibration Parameters 65

CHAPTER 1
INTRODUCTION

Particulate composites have become major components in many different aerospace applications in recent years. The addition of reinforcing particles into a polymeric matrix has resulted in increased material properties enabling superior materials than before [21, 51, 65, 19, 68, 9, 40, 48, 23, 67]. Many factors such as the particle material, shape and size can have a significant impact on the overall material properties of the composite [9, 12, 16, 37, 15, 60]. Efforts to understand the effect of these parameters on the material properties have been made using theory, simulation and experiments. Measurements of mechanical improvements have generally been limited to the effect on bulk properties from varying reinforcement parameters. Both piezospectroscopy (PS) and synchrotron X-ray diffraction (XRD) present the capability to directly measure stress within the particle in response to changes in external load on the composite. In order to gain a better understanding of the effect of particle size and shape, load transfer between the matrix and particle is studied here in a novel way, using piezospectroscopy. The results are compared to experimental data gathered using XRD and with theoretically load transfer models.

The focus of this chapter is to provide a general introduction to particulate composites and a background on all relevant topics. Background information on the effect of different reinforcement parameters is studied using theory, simulations and experiments. In addition, a background on specifically alumina particulate composites and an introduction to the experimental techniques used here, piezospectroscopy and X-ray diffraction, is given. Finally, an overview of the research performed is presented, including descriptions of each chapter.

1.1 Motivation and Background

Composites have revolutionized the aerospace industry with the creation of materials that have enhanced mechanical [40, 5, 14, 19], thermal [45, 55] and electrical [17, 66] properties. In the field of composites, particulate composites are gaining attention because they have, in some cases, lowered composite costs [63] compared to composites made using fiber materials. Particulate composites are also easy to manufacture at low volume fractions and have been shown to enhance material properties [9]. For these reasons and others, particle reinforced composites are being considered for use in critical aerospace structures [21]. The consideration of these materials in the aerospace field motivates the thorough and systematic investigation of the enhanced properties of these materials. The specific parameters that cause these enhancements have been investigated primarily in three ways, by using theoretical models, simulations and by experiments.

1.1.1 Simulations

The effects of different reinforcing parameters have been studied in literature using simulation techniques. Many simulations investigate the failure of materials through analysis of representative volume elements (RVE). A RVE is defined as the smallest unit cell that can be used to describe the overall composite. As seen in Figure 1.1, the use of a RVE simplifies the geometry of a composite while still maintaining both the particulate and the matrix material properties.

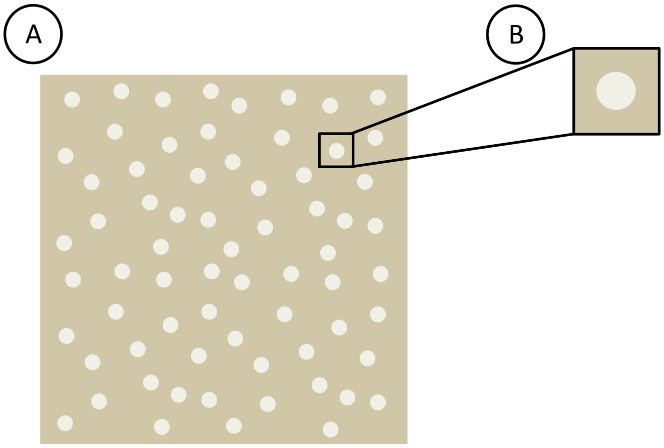

Figure 1.1: The Representative Volume Element (B) of a nanocomposite (A)

Finite element models (FEM) have been developed in recent years that model the effect of debonding on material properties [36] and have been shown to correlate closely with the existing theoretical models. The simulation of particle debonding is used to study the interface effect and shows the importance of particle to matrix adhesion. In addition to FEM studies, more recent studies using molecular dynamics (MD) models have been used to investigate nanocomposites [57, 52, 1, 15], which capture the nano-scale effects of particle reinforcements. Specifically, the effect of interacting particles [57] has been studied and the effect of filler size [1] has been investigated. The study on filler size demonstrated that elastic properties of nanocomposites are significantly improved with the reduction of particle size [1]. Although these simulations provide valuable insight to some reinforcement parameters, they are difficult to validate experimentally. Conventional material property testing techniques are not able to measure the stresses on the particle because they are on such a small scale. However, it is these stresses that are investigated using MD modeling. The novel experimental techniques of PS and XRD used here provide two methods of experimentally measuring forces at scales in the micro and nano range.

1.1.2 Theoretical Models

Theoretical models that predict the behavior of particulate composites have been in existence for a very long time. The Eshelby theory [24] was proposed in 1957 and is a fundamental theory in particulate mechanics that forms the framework for many other theoretical models. Even with the many assumptions of the Eshelby model, it has been successfully used to study load transfer in alumina nanoparticle composites [25]. Over the years other models have expanded upon Eshelby's original equations and modified them to study different reinforcing parameters [36, 27, 15]. A study focused on particle size and found that the tensile strength of particulate composites can be improved with decreasing particle size [15]. Another paper used the Eshelby-Mori-Tanaka approach to study many reinforcing factors of carbon nanotubes such as volume fraction of oriented CNTs, CNT distributions, shell angle and length to mean radius ratio [58]. The effect of interface debonding [62] was also studied using the Mori-Tanaka method [49]. It is apparent that theoretical models have been extremely useful in predicting the properties of certain composites. However, the assumptions of these models make experimental validation very difficult. As in any other field, a single unified theory has not yet been proposed but with the novel experimental validation techniques proposed here, further refinement of the existing models is possible.

1.1.3 Experiments

In addition to simulations and theoretical models, experimental methods are used to investigate particulate composites. Primarily bulk material properties have been studied thorough investigations of the overall composite material properties. Some studies have solely focused on the enhanced mechanical properties of adding particulate reinforcers to a matrix material. Nanometer sized TiO_2 particles in an epoxy matrix were used to increase composite scratch resistance [51], flexural strength, and toughness [65]. Also, SiC has been used in various matrices to increase the strength of the composite [19], and aluminum particles have been introduced to epoxy to increase fracture toughness [68]. In addition to the superior mechanical properties, the wide range of reinforcement parameters like different particulate filler materials, particle size, shape, and volume content allow for a high degree of customization of these particulate composites for desired mechanical properties.

Other experimental studies have focused on the effects of these different parameters. It is evident from the previous two sections that all these effects play critical roles in the performance of the overall composites. In a study using irregularly shaped particles, huge improvements in wear resistance were observed for the first time at low volume fractions [9]. Also, in a study on particle size, the tensile strength of the composite was shown to increase as the particle size decreased [15]. Additionally, single-particle composite tests have been used as a technique to measure residual stress effects [32] and they have been used to characterize interfacial strength [33], however both studies used visual observations and the stress in the particle was never quantified experimentally.

It is clear that these reinforcing parameters (particle size, shape, volume fraction, etc.) have a significant effect on the overall mechanical properties of particulate composites. However, additional information could be obtained by investigating the effects of mechanical loading on only the particulate inside of the composite, rather than the composite as a whole. The study of the loads (stresses and strains) experienced by the particles is possible using the experimental methods of PS, which can be used to measure the stress in the particle and XRD, which can be used to measure strain in the particle.

Both methods are used here to study load transfer between the particle and matrix while varying particle size.

1.1.4 Alumina Particulate Composites

This study focuses on the use of alumina reinforcement particles in a polymer matrix. The mechanical enhancements from alumina particles have been studied extensively in literature [30, 4, 6, 7, 11]. Alumina particulate composites have been shown to have particularly low densities and relatively high strengths [40]. They have been shown to increase wear resistance [9] and increase fracture toughness [48]. They have been also shown to increase strength [11, 2, 7, 56, 64]. For those reasons and others, alumina particles have been used in adhesives [28], as plasma sprayed coatings [23, 67], and various types of alumina composites have also been used as armor materials [18].

Here, spherical alumina particles are isolated in a polymer matrix forming a cylindrical sample. The samples are studied experimentally using PS and XRD, which can be used to determine stress and strain, respectively on the individual particle. Experimental measurements of stress and strain on the particle enable the study of load transfer between the matrix and particle because the applied load is known. Alumina has strong photoluminescence (PL) characteristics due to its natural occurring substitutional impurity of chromium ions Cr^{3+}. Once excited with a laser source, the alumina emits a spectrum with certain peaks, referred to as R-lines. When a force is applied to the alumina, these R-line peaks shift linearly with respect to the stress applied. The relationship between the R-line peak shifts and applied stress is known as piezospectroscopy. This optical property can be exploited to experimentally measure load transfer.

XRD can be used to determine strain based on changes in the crystal lattice spacing [39] which cause changes in the diffraction pattern. In addition to a very characteristic luminescent signature, alumina also has a distinct XRD pattern and has even been used as a calibrant material. In general, ex-situ studies on residual stresses are investigated with XRD. However, in-situ XRD studies [3, 54, 20, 59] can reveal material characteristics by simultaneous collection of XRD data with applied load, such as high resolution stress mapping of polycrystalline alumina samples [54].

Both of these experimental techniques are used here to investigate load transfer between the particle and matrix material. In addition, the simplified and ideal composite geometry allows for a more direct comparison to simulations and theoretical models such as the Eshelby theory [24].

1.2 Overview of Research

This chapter has served as an overview of the motivation and background for this work. A wide variety of particle parameters have been shown to affect the overall mechanical properties of particulate composites. By investigating the load experienced by the particle, a more complete understanding of the effect of these parameters can be achieved.

Experimental methods to quantify the loads experienced in the particle are sparse, however, two will be used here, PS and XRD. The XRD technique has been used before to investigate strains in many different materials. The use of alumina as the filler material here enables the use of PS as well. Using these experimental techniques, the micro-scale features of the load through the particle (XRD) and on the surface and sub-surface of the particle (PS) can be obtained.

Chapter 2 provides an in-depth background on the methods used in this study, both experimental and theoretical models. Starting with the basis for all the theoretical models used here, the Eshelby model, the chapter introduces the relevant equations [25] and derivations necessary. Following the theoretical models, both experimental methods are introduced, starting with the PS method, followed by the XRD method. All relevant equations and, derivations and theories necessary to fully understand the experimental data are given. The experimental methods are compared using the derived stress transfer ratio and are compared qualitatively as well.

Chapter 3 details the sample manufacturing process and both of the unique experimental setups. The process for isolating single alumina particles in polymer matrices is discussed and shown to not alter the integrity of the composite. After the manufacturing is described, the PS experimental setup at the University of Central Florida (UCF) is detailed along with an extensive description of the instruments used to collect the data. Lastly, the XRD experiment at the Canadian Light Source (CLS) is described and the procedure for collecting the diffraction rings is detailed.

Chapter 4 presents the results from the PS experiments. Plots of the R1 and R2 peak shift versus stress are provided for each sample and the PS coefficients are calculated. The hydrostatic stress ratio is calculated for each size class including the small, medium and large particles samples. Comparisons are made to determine the effect of particle size on load transfer. In addition, the particle shape effect is investigated qualitatively using the irregularly shaped particle samples. The chapter concludes with a discussion of the results and a comparison with literature.

Chapter 5 presents the XRD results in various ways. The diffraction patterns are initially analyzed for radius change to show the qualitative effect of increased load and location on the particle. The diffraction patterns are then run through a set of analysis codes that calculate the deviatoric strain each particle experiences. The chapter concludes with a qualitative comparison of the XRD results with the PS results.

The document closes with Chapter 6 in which some conclusions are drawn from this work. The XRD and PS techniques effectiveness in studying particle size is discussed. In addition, a future direction of the research is provided and additional, new and improved experiments are proposed.

CHAPTER 2
METHODS: PIEZOSPECTROSCOPY, THEORETICAL MODELS AND X-RAY DIFFRACTION

Throughout this work many different methods are used to obtain results and for analysis of the results. Theoretical models are used to develop a fundamental understanding of the mechanics and to compare the experimental results. Eshelby's equivalent inclusion idea [24] is described and the Mori-Tanaka method [49] are discussed. Piezospectroscopy (PS) and X-ray diffraction (XRD) are used to gain experimental insight into the load transfer between the particle and matrix. In this chapter, each topic is thoroughly described and the stress transfer ratio is derived using piezospectroscopic coefficients. This ratio is used to compare the experimental data with the theoretical models.

2.1 Piezospectroscopy

The alumina samples chosen for this study have a characteristic photoluminescent signature that enables piezospectroscopic studies using photo-stimulated luminescence spectroscopy (PSLS). The signature stems from the naturally occurring chromium doping of α-alumina particles. Once excited by a laser source, the Cr^{3+} ion substitutional impurities fluoresce and have distinct spectral peaks at $14403cm^{-1}$ and $14432cm^{-1}$ which correspond to the R1 and R2 peaks. These two intense peaks are seen clearly through a spectrometer as shown in Figure 2.1. As the alumina is subjected to compressive loads, the crystal lattice is strained and the spectral position of the peak shifts to lower wavenumbers. The relationship between the peak shifts and stress is known as piezospectroscopy [29].

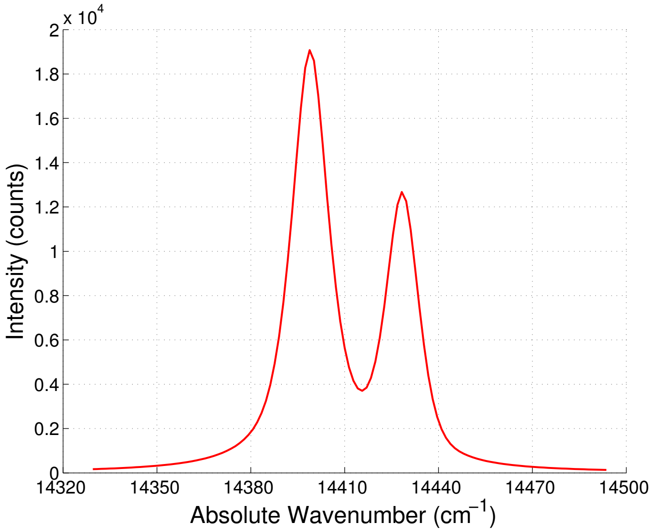

Figure 2.1: R1 and R2 peaks for α-Alumina

The piezospectroscopic coefficient is seen in Equation 2.1 and relates the frequency shift to the applied stress. $\Delta\nu$ is the frequency shift, π_{ij} is the piezospectrocopic coefficient, and σ_{ij} is the stress. For a single crystalline sample, assuming the crystallographic orientations are known, both the hydrostatic and deviatoric stress can be obtained. However, when alumina is a polycrystalline material the piezospectroscopic effect is averaged over all the randomly oriented grains that are excited by the laser source. By averaging Equation 2.1 over all possible crystallographic orientations the peak shift is found to be a function of only the hydrostatic stress. This results in a new Equation 2.2 [46].

$$\Delta\nu = \Pi_{ij}\sigma_{ij} \tag{2.1}$$

$$\Delta\nu = \frac{1}{3}\Pi_{ii}\sigma_{jj} \tag{2.2}$$

Figure 2.2 shows the shifting of the R-lines with applied stress. The data from an entire loading cycle or map can be compiled into a peak shift versus stress plot also seen in Figure 2.2. A linear curve fit can be performed to determine the PS coefficient.

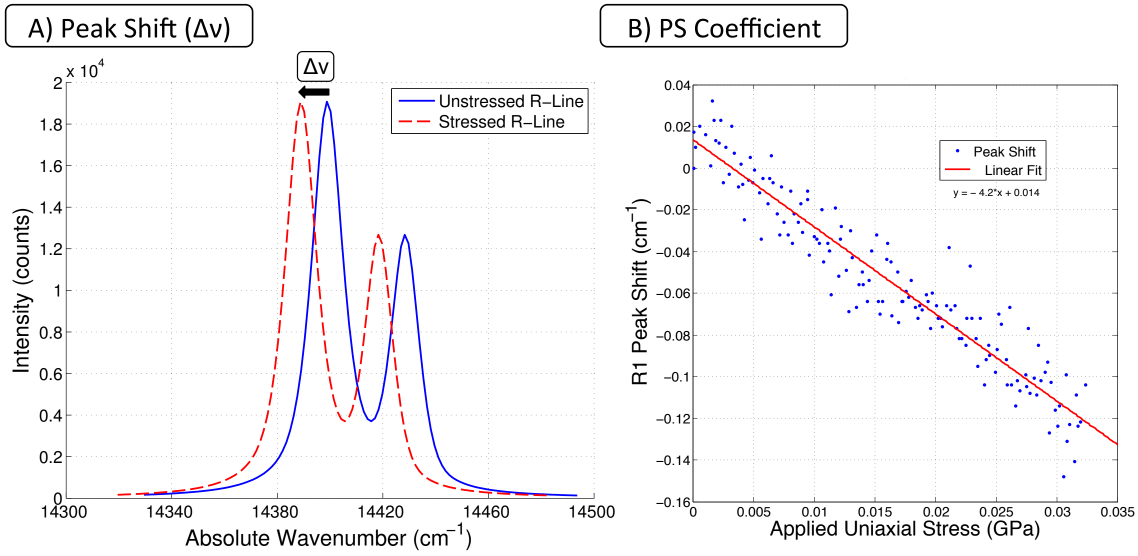

Figure 2.2: A spectral peak shift with applied load (A) and a peak shift versus stress plot (B)

PSLS has been used to study the effect of particle dispersion and volume fraction in alumina nanocomposites [60]. In Stevenson's work, the R1 and R2 peaks were plotted versus applied stress and the resulting PS coefficients were observed. It was shown that an increase in volume fraction resulted in an increased PS coefficient, which shows that measurement of the loads experienced by just the particles can be accomplished using PS. For the single particle composites used here:

$$\Delta\nu = \Pi_c \sigma_{applied} \tag{2.3}$$

In addition to the PS coefficient, by equating Equation 2.1 with Equation 2.3, the hydrostatic stress ratio can be determined which relates the applied stress and measured PS coefficient with the hydrostatic stress on the particle. As seen in Equation 2.4, this relationship can be used to study load transfer in single particle composite samples [22].

$$\frac{\frac{1}{3}\sigma_{ii}}{\sigma_a} = \frac{\Pi_c}{\Pi_{ii}} \tag{2.4}$$

2.2 Theoretical Models

Theoretical models that predict the behavior of particulate composites have been in existence for a very long time. The Eshelby theory [24] was proposed in 1957 and is a fundamental theory in particulate mechanics. Although other models existed before, Eshelby's model described a new approach to inclusion problem which involved, in his own words, "a simple set of imaginary cutting, straining and welding operations." [24].

By removing the inclusion and solving the problem using superposition, Eshelby found that the stress in an ellipsoidal inclusion is uniform. This results in spherical inclusions, such as the ones used here, having just one unique stress value. This can be compared to the hydrostatic stress in the particle obtained experimentally from PS measurements.

The classical Eshelby model used in this work has several assumptions:

1. Only a single particle is considered
2. The particle is perfectly spherical
3. The particle is perfectly bonded to the matrix
4. Both the particle and matrix materials are isotropic

Many of these assumptions are represented quite accurately by the manufactured samples. This is done by design to allow for a more direct comparison. The process of calculating the stress in the particle starts by defining three strain values, e (strain from the filler), e^o (strain on the matrix from applied load), and e^* (equivalent eigenstrain of the inclusion problem) [50]. With the strain defined, the stress can be calculated using Equation 2.8 and 2.9, where C represents the stiffness tensor and S represents the Eshelby tensor [50].

$$e = Se^* \tag{2.5}$$

$$e^o = (C^m)^{-1}\sigma^m \tag{2.6}$$

$$e^* = -[(C^p - C^m)S + C^m]^{-1}(C^p - C^m)(C^m)^{-1}\sigma^m \tag{2.7}$$

$$\sigma^p = C^m(e^o + e - e^*) \tag{2.8}$$

$$\sigma_{ii}{}^p = trace(\sigma^p) \tag{2.9}$$

Using Eshelby's model it is possible to predict the hydrostatic stress ratio and compare it with experimental values obtained from the PS experiments [25]. However, the model is very limited in a practical sense because it can only handle a single particle in an infinite matrix. As a result, there have been many variations of the Eshelby model such as the work by Mori and Tanaka [49] which accounted for multiple inclusions in a finite domain. The equivalent inclusion average stress method is based on the equivalent inclusion idea from Eshelby and the average stress in the matrix from Mori-Tanaka [58]. Even further modification of the theory is necessary if effects from particle size variation are to be accounted for. More recently, an extension of the Mori-Tanaka method was able to account for particle size and found, among other things, that the effect of particle size is amplified with stiffer particles [47], such as the ceramic particles used here.

2.3 X-Ray Diffraction

X-ray diffraction (XRD) is a technique that is used to investigate the atomic structure of a material. The relative intensity and spatial distribution of scattered X-rays essentially represents the signature of the material. Since the atomic structure for alumina is so unique, its signature diffraction pattern is very pronounced and has a suggested use as a calibrant during X-ray diffraction experiments.

The scattering of X-rays was first observed by Max von Laue in 1912 [34]. This first observation of X-ray diffraction paved the way for what has today become a large part of many different scientific fields. The diffraction itself occurs when the X-rays scatter as they interact with the electrons surrounding an atom [34]. The geometrical conditions that must be satisfied for diffraction to occur in a crystal were first established by Bragg. In cubic systems the spacing of these planes, d_{hkl}, is related to the lattice constant, a as stated in Equation 2.10.

$$d_{hkl} = \frac{a}{\sqrt{h^2 + k^2 + l^2}} \tag{2.10}$$

Bragg's Law describes the angular position of the diffracted beam in terms of λ and d_{hkl}.

$$n\lambda = 2d_{hkl}sin\theta \tag{2.11}$$

In most instances of interest, $n = 1$ and accordingly, Bragg's Law is:

$$\lambda = 2d_{hkl}sin\theta \tag{2.12}$$

Single dimension (1-D) detectors have been the main source of data collection in the field of X-ray diffraction. Many different X-ray diffraction applications, such as phase identification, orientation identification, residual stress measurement, crystal size, and percent crystallinity, all incorporate this mode of collecting data [38]. However, with the recent development of powerful X-ray beams from third generation synchrotrons, a high-energy XRD technique based on transmission geometry has been developed that allows the use of two-dimensional (2D) detectors. Only a handful of these synchrotron radiation source facilities exist but they provide the high energy X-rays necessary for high resolution strain measurements.

Strain measurement using XRD is based on the fundamental relationship between the strain and the change in the Debye-Scherrer diffraction cones. The strain free state results in a diffraction pattern in the form of a perfect circle. As the sample is loaded, the strain in the crystal lattice increases which causes changes in the spacing between planes. This strain in the crystal lattice causes the diffraction pattern to distort and form an ellipse. By quantifying the change in radius, Equation 2.13 can be used to yield strain information.

$$\epsilon = \frac{(d - d_0)}{d_0} \tag{2.13}$$

CHAPTER 3
SAMPLE MANUFACTURING, AND EXPERIMENTAL SETUP

Two main experiments were conducted as part of this work, a piezopectroscopic experiment at the University of Central Florida (UCF) and an X-ray diffraction (XRD) experiment at the Canadian Light Source (CLS). Both experiments used single particle alumina-epoxy samples manufactured at UCF. This chapter details the process for manufacturing the single-particle samples and explains the different experimental setups used at UCF and CLS.

3.1 Sample Geometry and Manufacturing

The samples were broken up into four main classes, samples with large, medium, small and irregularly shaped particles. Two different sample diameters, $6mm$ and $7mm$ were used and three samples for each class were manufactured. The samples contained a single alumina particle embedded within an epoxy matrix. The sample geometry allowed for isolation of the particle size effect and shape effects. It also adheres, as best as possible, to the four assumptions of the classical Eshelby model presented in Chapter 2. Each sample was fabricated using α-alumina spherical particles from Christy Catalytics and Epon 862 (Bisphenol-F type) epoxy cured with Epikure-W.

3.1.1 Alumina Particles

Alumina particles were chosen as the filler material due to their high strength, intense photoluminescent characteristics and intense diffraction pattern. As mentioned in Chapter 2, the photoluminescence stems form the chromium ion impurity in alpha phase alumina. For this reason, α-alumina spherical particles from Christy Catalytics were used for this study. Specifically, T-99 PROX-SVERS Inert Catalyst Support Balls were used which are composed of greater than 99% sintered alpha-alumina with very low impurity levels and have ultra low porosity and very high density. Their spherical shape and composition further motivated their use in this work. A chemical analysis done by the manufacturer showed 99.5% alumina (Al_2O_3), less than 0.15% silica (SiO_2), less than 0.1% iron (Fe_2O_3) and less than 0.5% soda (Na_2O). The spheres had varying diameters ranging from $1mm$ to $3mm$.

3.1.2 Particle Size

Without the use of a powerful microscope or Scanning Electron Microscope (SEM), locating and constraining single nanoparticles is challenging because of their size. Macro scale studies in this initial research effort are limited to larger particles in the micro to millimeter range, which allow for easy manufacturing and handling of the samples. In addition, the larger particles were perfectly spherical as opposed to the agglomerated nanoparticles as seen in Figure 3.1. This spherical shape allowed for a more direct comparison to theoretical models that assume perfect spherical inclusions. The dimensions of the particle with respect to the matrix were kept small to avoid edge effects so that the particle would experience a uniform stress state. This was also done to more closely approximate the infinite matrix assumption of Eshelby's model. The diameter of the overall samples were $6mm$ and $7mm$. Using a simple finite element model, it was estimated that a particle diameter to sample diameter ratio of 4:1 would be necessary to avoid edge effects.

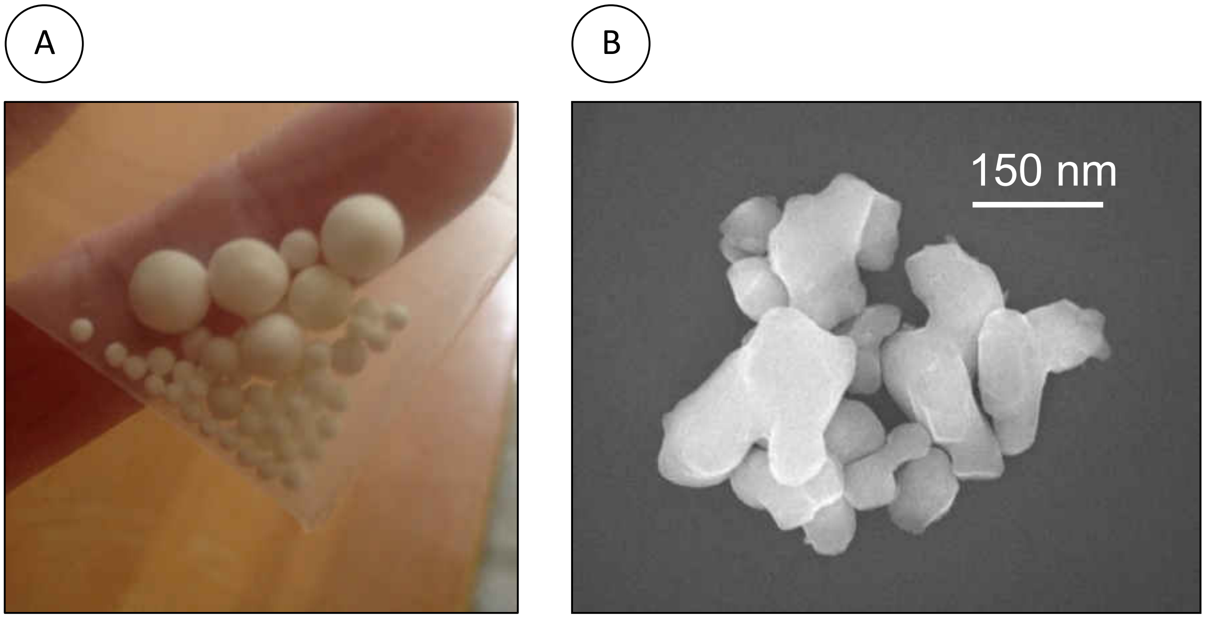

Figure 3.1: A) Spherical millimeter alumina particles and B) non-spherical alumina nanoparticles

3.1.3 Irregular Shape

A qualitative investigation of particle shape is done in this study by crushing the alumina spheres used for the particle size investigation using two aluminum plates and a mallet. The spherical particles were placed in between the plates and crushed using the mallet. The resulting pieces were photographed using a microscope and precise measurements of the largest dimension of the particles were made. As seen in Figure 3.2 the particles were no longer spherical and instead were irregular in shape. Samples were manufactured using these alumina shards in order to qualitatively investigate the differences between spherical and non-spherical inclusions.

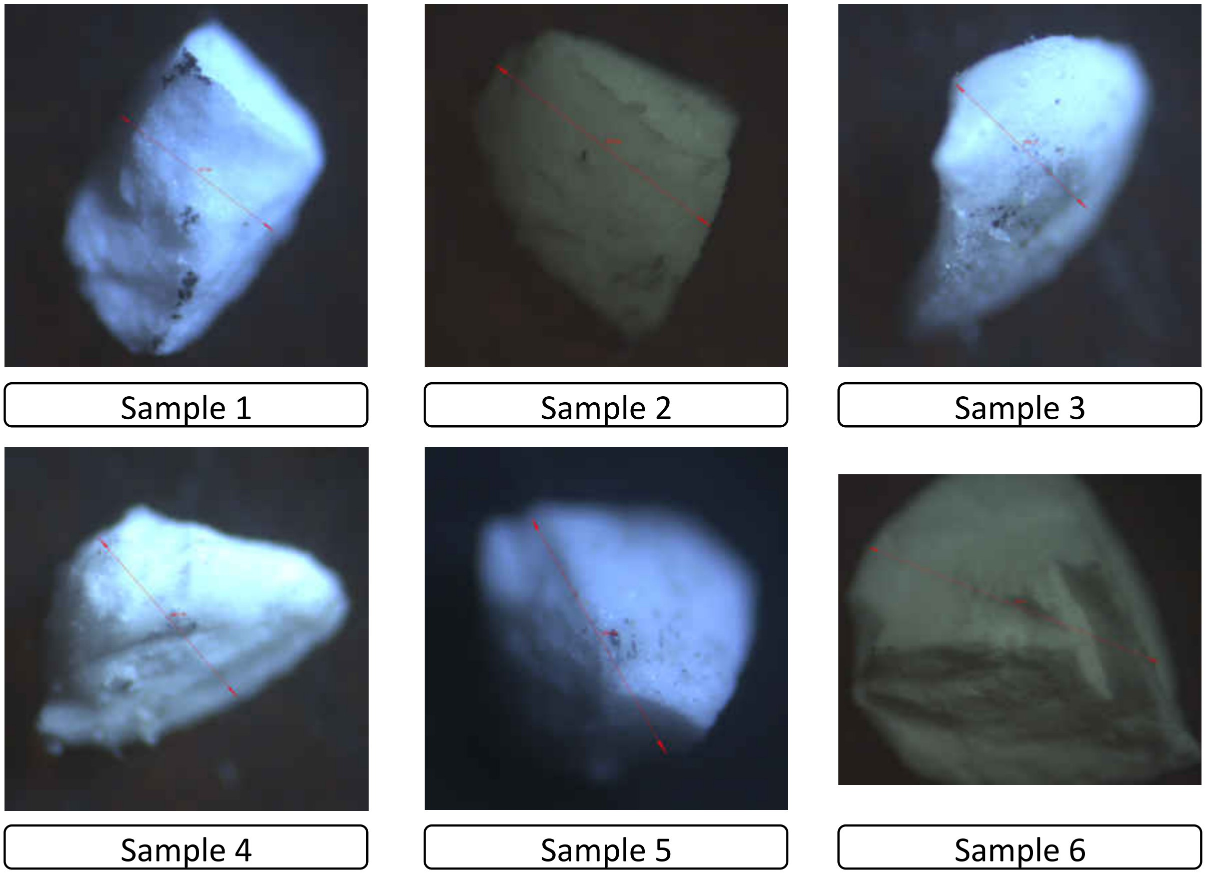
Sample 1
Sample 2
Sample 3
Sample 4
Sample 5
Sample 6

Figure 3.2: Images of the irregularly shaped particle under 10x magnification

3.1.4 Method for Suspending Particle in Matrix

To manufacture the isolated particle samples, an aluminum mold was created by drilling holes in a piece of stock 6061 aluminum that was $38mm$ thick. The diameter of the holes were chosen to match the desired diameter of the samples, $6mm$ and $7mm$ and the thickness was chosen to allow for the samples to be machined down to a 2:1 aspect ratio.

Figure 3.3 shows the process used for isolating the single alumina sphere in the epoxy matrix. The process started by partially curing only half of the epoxy in the mold to create a plateau for the alumina particle to rest on. Once the first layer of epoxy was cured for 2 hours, a single alumina particle was placed into each hole in the mold. The mold was then filled completely with epoxy and fully cured. In addition to a schematic of the manufacturing process, an example of the final extracted sample can be seen in Figure 3.3.

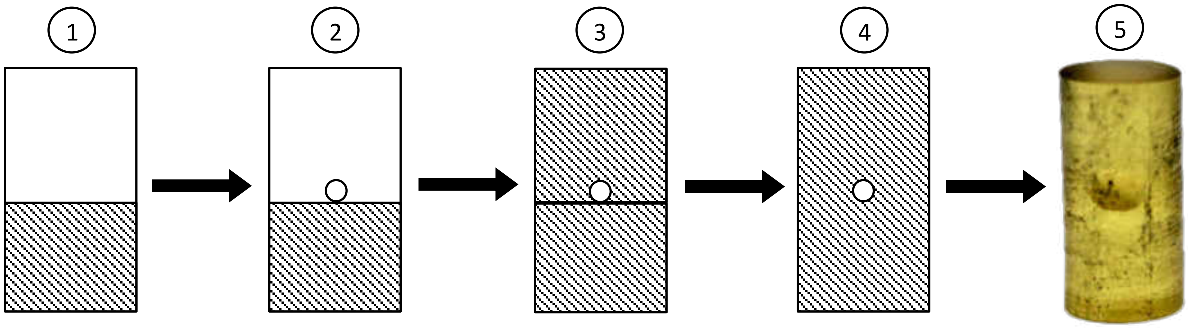

Figure 3.3: 5-step manufacturing process showing 1) mold filled half-way with epoxy, 2) placement of a single alumina particle, 3) mold filled entirely with epoxy, 4) fully cured sample, and 5) final sample extracted from mold

3.1.5 Final Samples

During manufacturing, some samples generated a large amount of micro bubbles. Other samples adhered to the aluminum mold and as a result, were damaged during extraction.

Additionally, some samples had very opaque outer coatings due to damage during extraction from the mold. A list of the final samples can be found in Table 3.1. A total of six irregularly shaped particle samples and nine spherical shaped particle samples were used in this study. Although other samples were manufactured, the samples listed in the table showed the best uniformity and clarity.

Table 3.1: List of Samples

Sample Number	Matrix Diameter (mm)	Particle Diameter (mm)	Class
1	6.14	0.678 ± 0.100	Irregular
2	6.14	0.764 ± 0.100	Irregular
3	6.14	0.580 ± 0.100	Irregular
4	6.14	0.641 ± 0.100	Irregular
5	6.14	0.808 ± 0.100	Irregular
6	6.14	1.400 ± 0.100	Irregular
10	7.14	1.287 ± 0.026	Small
11	7.14	1.260 ± 0.011	Small
12	7.14	1.287 ± 0.047	Small
13	7.14	1.453 ± 0.058	Medium
14	7.14	1.440 ± 0.071	Medium
15	7.14	1.420 ± 0.057	Medium
16	7.14	1.687 ± 0.046	Large
17	7.14	1.770 ± 0.023	Large
18	7.14	1.873 ± 0.036	Large

3.2 Experimental Setup

Two separate experimental methods were used in this work, a photo-stimulated luminescent spectroscopy (PSLS) setup and an X-ray diffraction (XRD) setup. The PSLS experiments were conducted at the University of Central Florida (UCF) College of Engineering and Computer Science (CECS) in the department of Mechanical and Aerospace Engineering (MAE). The XRD experiments were conducted at the Canadian Light Source (CLS) Very Sensitive Elemental and Structural Probe Employing Radiation from a Synchrotron (VESPERS) beamline.

3.2.1 Photo-Stimulated Luminescent Spectroscopy

Photo-stimulated luminescent spectroscopy is used to study load transfer in the single particle alumina-epoxy samples. Figure 3.4 shows the portable spectroscopy system that consists of 7 major components. The components are a spectrograph, Charge-Coupled Device (CCD), X-Y-Z stage, laser, fiber optics, computer and support equipment including a tripod, moving cart and rolling case. The laser is used to excite the alumina via the fiber optics. The response is then collected through the fiber optics and passed through the spectrometer. The spectrometer separates the light into distinct wavenumbers and the CCD captures the scattered light. The captured image is saved by the computer and the computer is also used to manage and specify certain parameter such as exposure time and the spectrometer grating center wavelength.

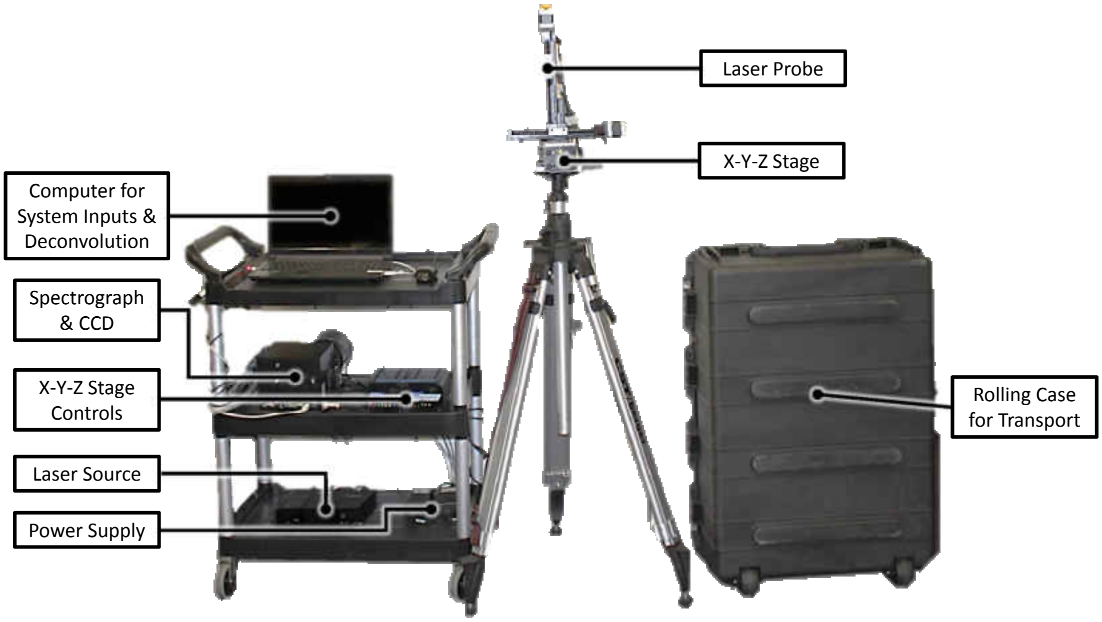

Figure 3.4: The portable spectroscopy system

A schematic representation of the portable spectroscopy system is visible in Figure 3.5. This figure shows a clearer image of the data path from the optics, to the saved image on the computer.

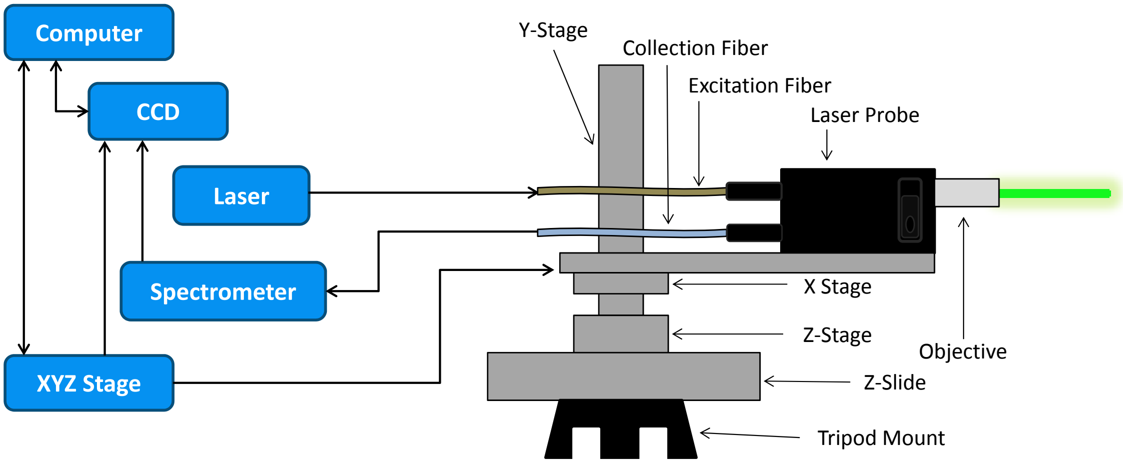

Figure 3.5: Portable spectroscopy system schematic

The collected emission spectra were post processed to reveal peak shift information. Each spectra was deconvoluted and fitted to a pseudo-Voigt function, as seen in Figure 3.6, using a least squares routine to reveal more accurate R1 and R2 peak positions. These peak positions were then plotted versus the applied stress. A linear fit is performed and the resulting slope is the PS coefficient.

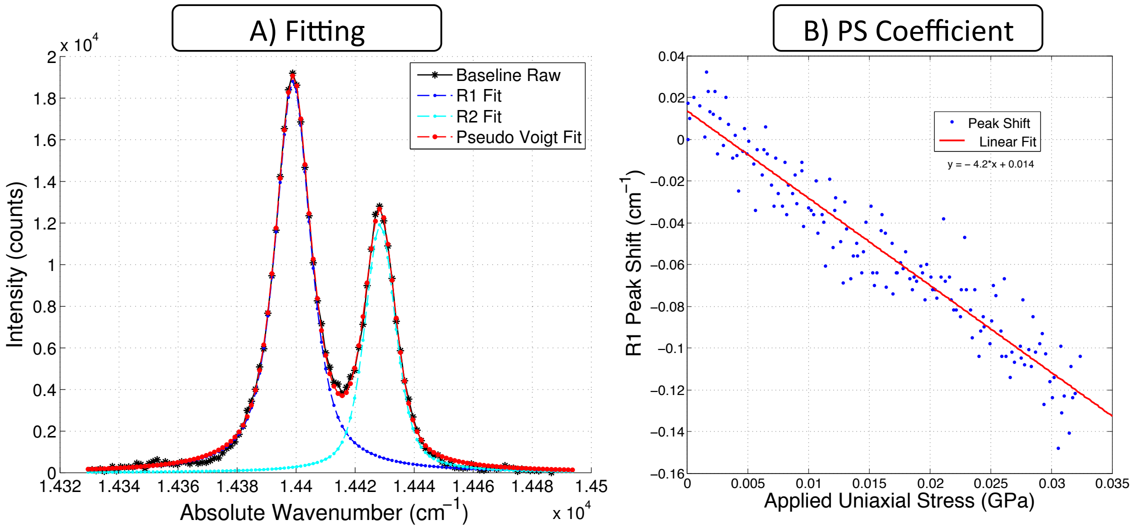

Figure 3.6: Deconvolution and fitting of the two peaks (A) and PS coefficient determination (B)

Figure 3.7 shows the entire experimental setup that consists of compressing the cylindrical samples using a mechanical load frame while simultaneously collecting PSLS data using the portable spectroscopy system.

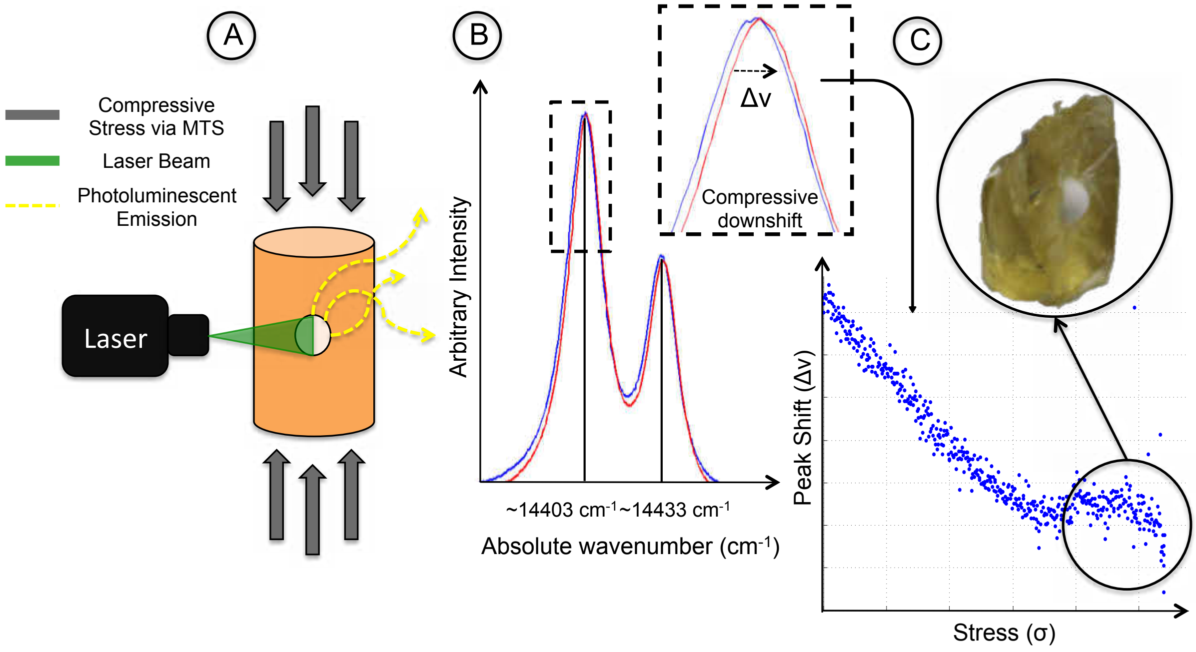

Figure 3.7: PSLS experimental setup and data analysis including A) loading the samples via a mechanical load frame, B) peak determination using a least squares fit of the raw data and C) plotting of the peak shift data for a sample until failure

3.2.2 X-Ray Diffraction

In addition to the experimental setup at UCF, XRD data was collected at CLS. The manufactured samples were loaded using a miniature mechanical load frame that was designed and manufactured specifically to be compatible with the beamline setup at the VESPERS beamline. The load frame, as seen in Figure 3.8, was able to induce compressive loads of up to 1200N. The load information was collected using an Omega load cell and monitored using a computer inside the experimental hutch at CLS.

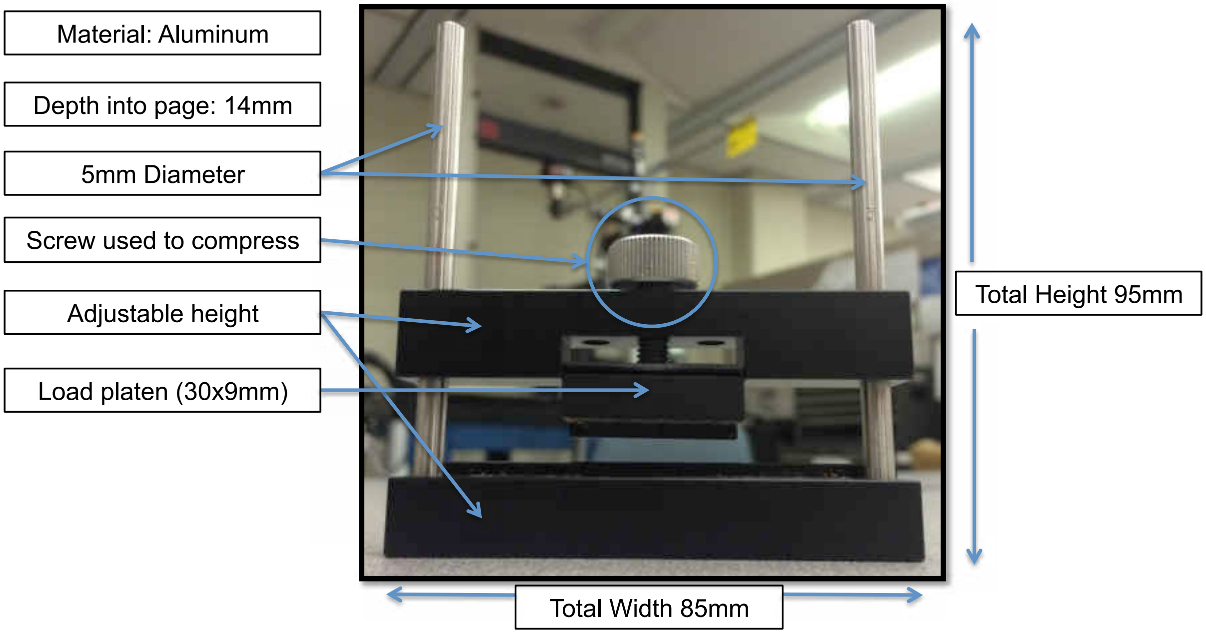

Figure 3.8: Miniature mechanical load frame used at the Canadian Light Source

The experimental hutch can be seen in Figure 3.9 where a schematic is presented to show the through transmission geometry of the X-ray diffraction setup. The hard X-ray beam passes through the sample and diffracts resulting in a diffraction pattern that is captured by the 2D detector.

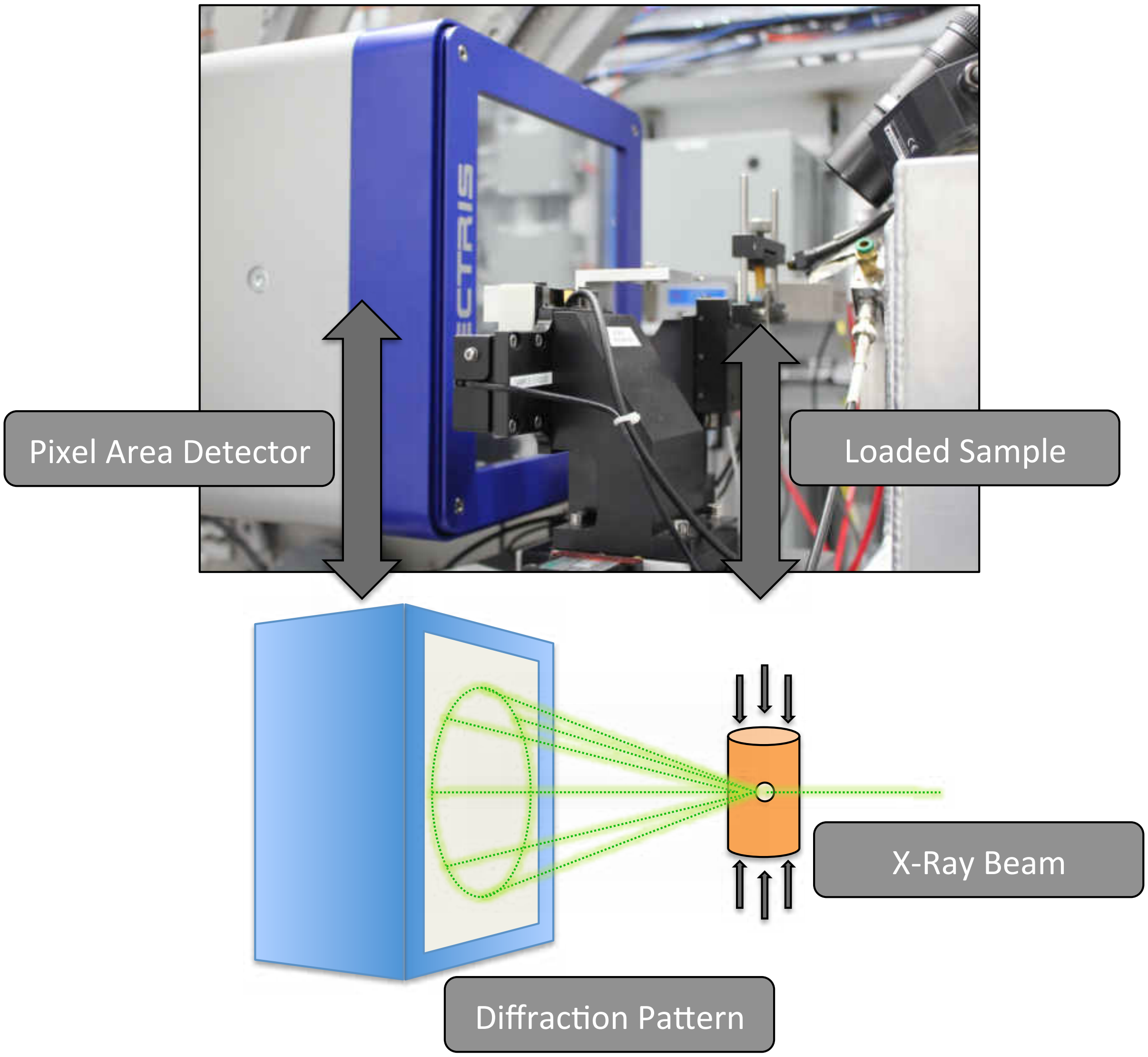

Figure 3.9: Through transmission X-ray diffraction

The overall experimental setup can be seen in Figure 3.10 where the miniature load frame is seen applying a compressive load to the sample, while the hard X-ray beam is producing diffraction rings captured by the single-photon counting pixel area detector. The VESPERS beamline was setup for through transmission XRD using their Pilatus 1M (single-photon counting) Detector System consisting of 10 modules. The focused hard X-ray beam was roughly $4\mu m$ by $4\mu m$ with an energy of $17keV$. Each sample was placed in the loading frame and the data collection system for the load measurement device was started. The load data for every experiment was collected by a data acquisition device and was recorded at a rate of $10Hz$. Diffraction rings were collected at 3 different load steps for each sample with the maximum load not exceeding $1200N$. In addition to the samples, an alumina powder diffraction pattern was also collected for calibration purposes. The calibration parameters, obtained using Fit2D [31], can be found in Table 5.8.

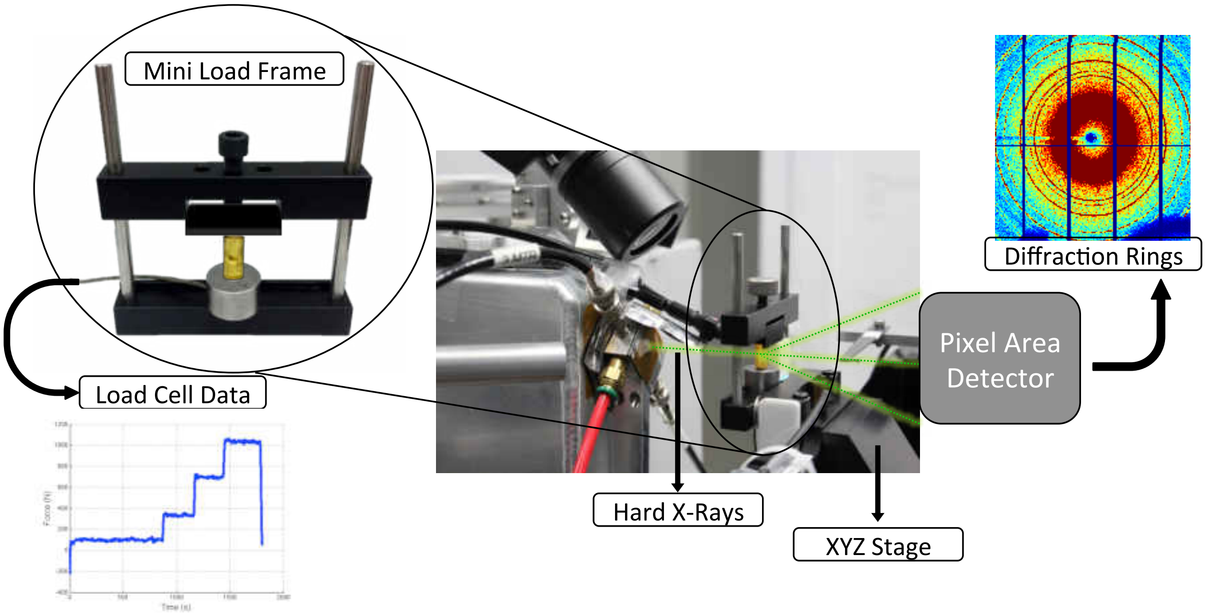

Figure 3.10: In-situ data collection using X-ray diffraction and the miniature load frame at the VESPERS beamline

Table 3.2: Beam, Detector and Calibration Parameters

Parameter	Value
Beam Energy	$17855eV$
Beam Size	4x4μm
Detector Size	981x1043 $pixels$
Detector Pixel Size	$172\mu m$
Sample to Detector Distance	$171.6mm$
Beam Center	$(521.46mm, 517.01mm)$
Tilt (Axis of Rotation, Rotation)	$(27.101°, 0.498°)$

CHAPTER 4
PIEZOSPECTROSCOPIC ANALYSIS OF ALUMINA-EPOXY SAMPLES

In this chapter, all the photo-stimulated luminescent spectroscopy results for the single particle alumina-epoxy specimens are presented. This technique has been used [60] to study the effects of particle dispersion and volume fraction. The bulk of this work is focused on studying the particle size effect using piezospectroscopy. This is accomplished by using samples that were manufactured in-house, and the unique portable spectrometer system developed at UCF. The spectral shifts are monitored as the samples are loaded and this data is used to calculate a piezospectroscopic (PS) coefficient. These coefficients are then used to calculate load transfer between the matrix and particle. The load transfer characteristics of these composites are used to investigate the effect of particle size. In addition to particle size, particle shape effects were investigated using irregularly shaped particles.

4.1 Particle Size Studies

The particle size effects are studied here using data collected from the portable spectroscopy system. The experiment was conducted in the manner presented in Chapter 3 and a summary of the samples used is provided in Table 4.1. The samples were broken up into three sets of three by grouping the small, medium and large particle samples together. All the analyzed data is presented here, where plots of the R1 peak shift versus stress are shown. The data displayed is smoothed by averaging 15 points together in order to reduce the density of the data. For all the samples, the data in the linear range, up to $50MPa$ was investigated.

Table 4.1: Summary of Samples

Number of Samples	Class	Range of Particle Size
3	Small	$1.2 - 1.3\ mm$
3	Medium	$1.4 - 1.5\ mm$
3	Large	$1.6 - 1.7\ mm$

4.1.1 Small Particle Size Results

The first experiments conducted were on the smaller particle samples. Figures 4.1, 4.2, and 4.3 show the R1 and R2 peak shift versus applied stress plots. Both Samples 10 and 11 show similar, expected trends and the R1 and R2 peak positions shift linearly with stress. However, Sample 12 shows anomalous behavior and did not experience the same linear behavior as the other samples in this group. This could be due to a number of reasons such as manufacturing defects, or the particle may have displaced outside of the laser dot. As a result, Sample 12 is not included in the calculations later in this chapter.

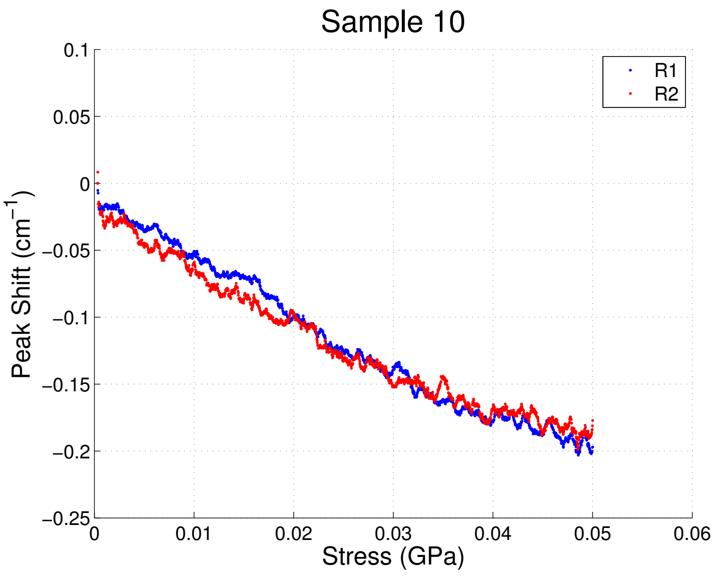

Figure 4.1: Sample 10 R1 and R2 Peak Shift versus Stress

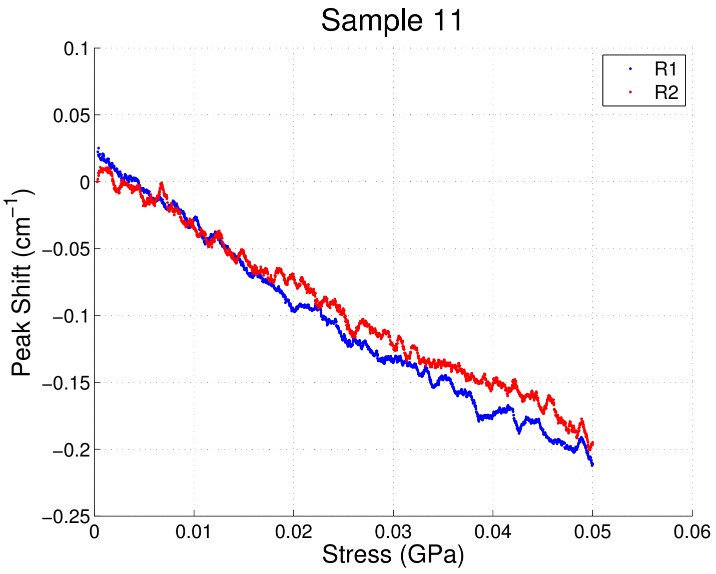

Figure 4.2: Sample 11 R1 and R2 Peak Shift versus Stress

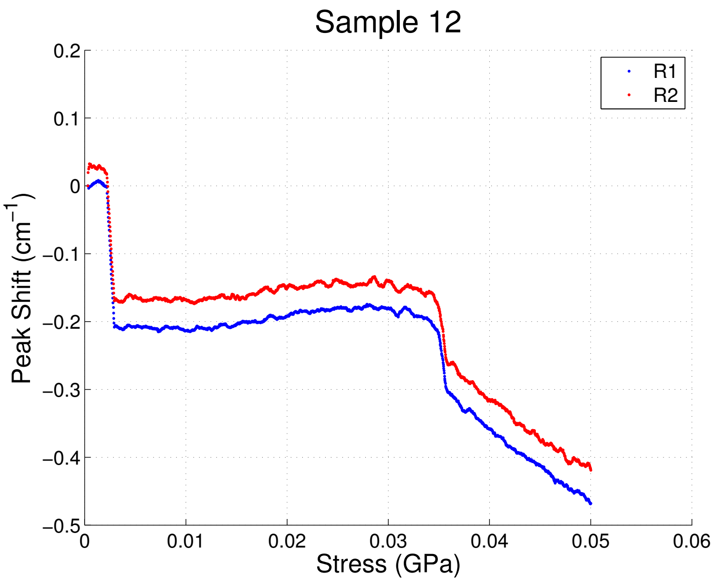

Figure 4.3: Sample 12 R1 and R2 Peak Shift versus Stress

With the data collected and the relationship between the applied stress and the peak shift quantified, the next step was to calculate the PS coefficients. A linear curve fit was performed on each plot and the resulting R1 and R2 PS coefficients are presented in Table 4.2. The average R1 PS coefficient for the small samples was determined to be $-4.214 \pm 0.621\ cm^{-1}/GPa$ using a 95% confidence interval. This value will later be used to calculate the hydrostatic stress transfer ratio during the load transfer analysis.

Table 4.2: R1 and R2 PS Coefficients (Small Samples)

Sample Number	R1 PS Coefficient	R2 PS Coefficient
10	$-3.898\ cm^{-1}/GPa$	$-3.975\ cm^{-1}/GPa$
11	$-4.531\ cm^{-1}/GPa$	$-5.674\ cm^{-1}/GPa$

4.1.2 Medium Particle Size Results

Next, the medium particle size samples were tested which included Samples 13, 14 and 15. The same process was undertaken with these samples and the R1 and R2 park shift versus stress plots are shown. For this group of Samples, due to a lack of trend in the anomalous data shown, Sample 13 was excluded from analysis.

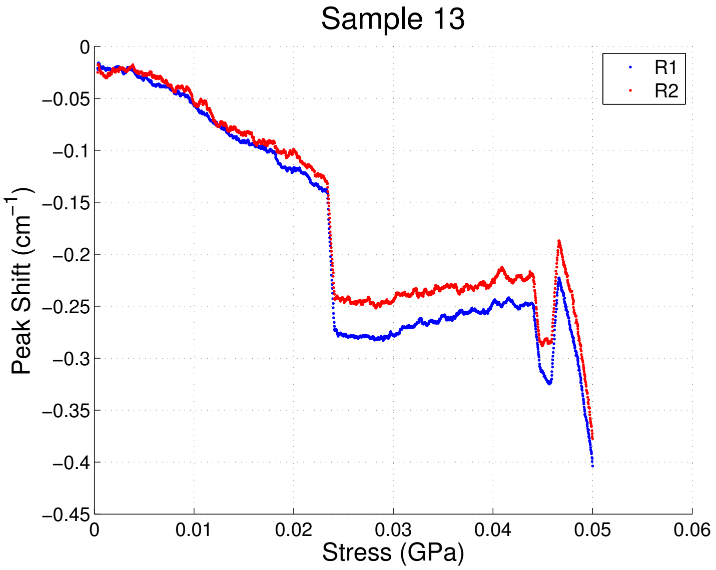

Figure 4.4: Sample 13 R1 and R2 Peak Shift versus Stress

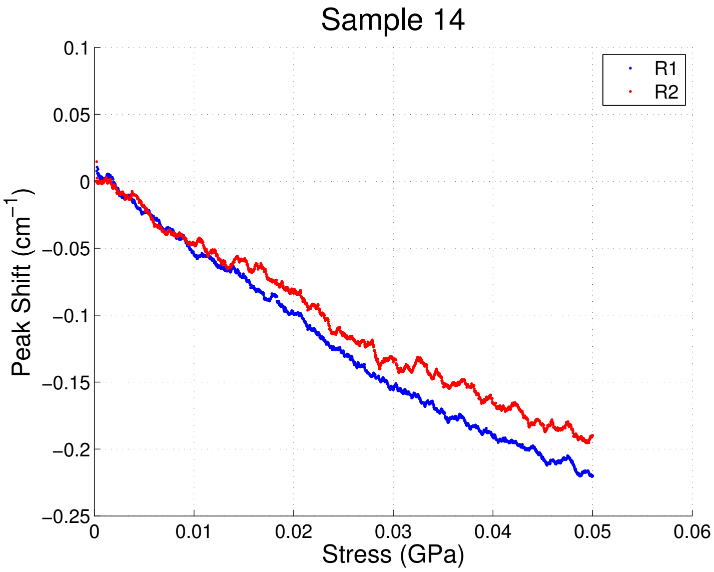

Figure 4.5: Sample 14 R1 and R2 Peak Shift versus Stress

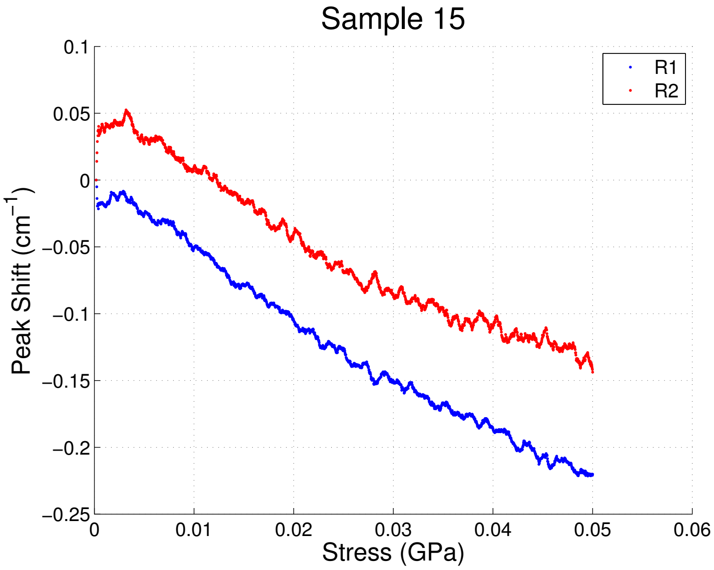

Figure 4.6: Sample 15 R1 and R2 Peak Shift versus Stress

Analysis of the data provides the R1 and R2 PS coefficients which are presented in Table 4.3. The average R1 PS coefficient for the medium samples was determined to be $-4.558 \pm 0.133\ cm^{-1}/GPa$ using a 95% confidence interval.

Table 4.3: R1 and R2 PS Coefficients (Medium Samples)

Sample Number	R1 PS Coefficient	R2 PS Coefficient
14	$-4.626\ cm^{-1}/GPa$	$-4.003\ cm^{-1}/GPa$
15	$-4.490\ cm^{-1}/GPa$	$-3.857\ cm^{-1}/GPa$

4.1.3 Large Particle Size Results

Lastly, the large particle size samples were tested which included Samples 16, 17 and 18. As seen in Figure 4.7, the slopes of the R1 and R2 peak shift versus stress plots for Sample 16 were much smaller in magnitude when compared with Samples 17 and 18 in Figures 4.8 and 4.9, respectively. Although Sample 16 showed a much lower slope than Samples 17 and 18, it is still included in the analysis because the data did show a linear trend. From the scales on the plots, it can already be observed qualitatively that the larger particles are experiencing greater peak shifts.

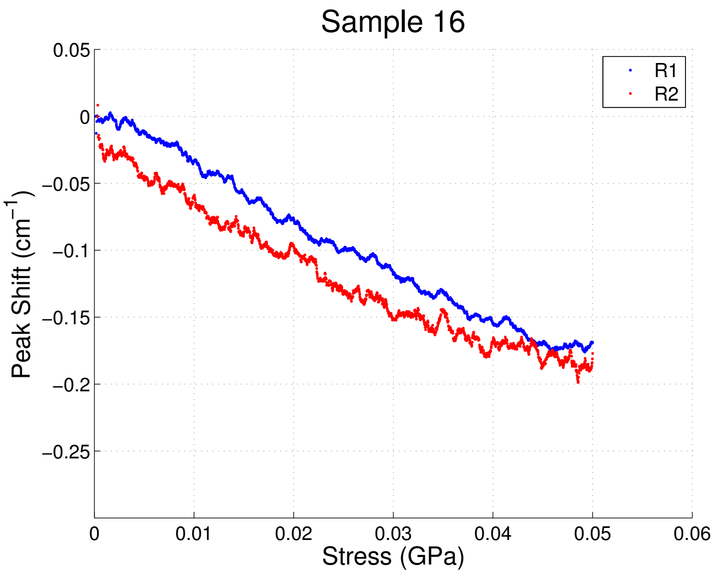

Figure 4.7: Sample 16 R1 and R2 Peak Shift versus Stress

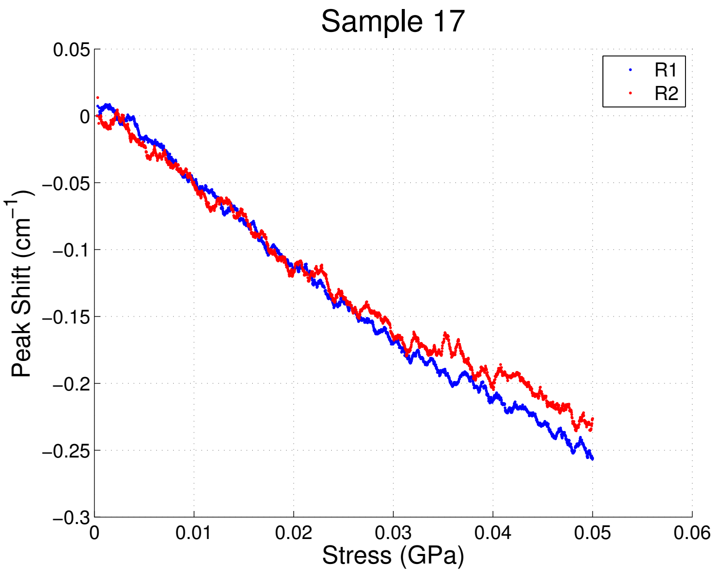

Figure 4.8: Sample 17 R1 and R2 Peak Shift versus Stress

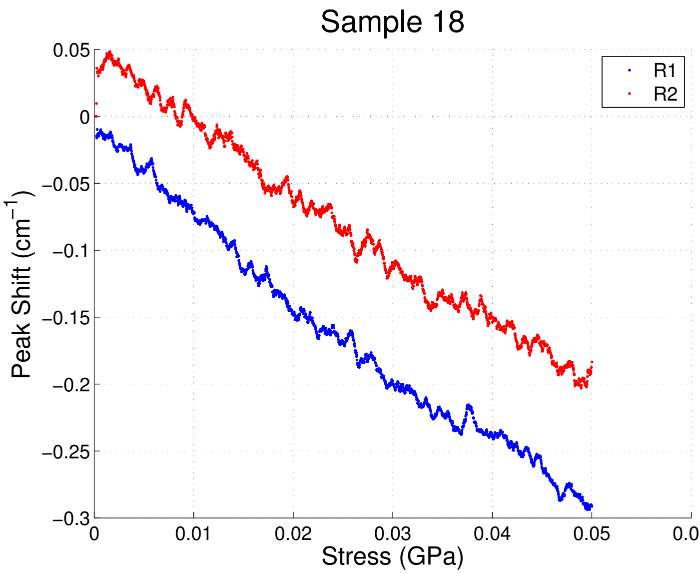

Figure 4.9: Sample 18 R1 and R2 Peak Shift versus Stress

The R1 and R2 PS coefficients are presented in Table 4.4. Also, by using a 95% confidence interval, the average R1 PS coefficient for the large samples was determined to be $-5.49 \pm 0.221\ cm^{-1}/GPa$.

Table 4.4: R1 and R2 PS Coefficients (Large Samples)

Sample Number	R1 PS Coefficient	R1 PS Coefficient
16	$-3.824\ cm^{-1}/GPa$	$-3.429\ cm^{-1}/GPa$
17	$-5.386\ cm^{-1}/GPa$	$-4.722\ cm^{-1}/GPa$
18	$-5.611\ cm^{-1}/GPa$	$-4.970\ cm^{-1}/GPa$

4.1.4 Summary of Particle Size Results

The applied uniaxial load on the composite translates into a multiaxial stress state experienced by the particle, which has a higher modulus than the matrix. With the smaller cross section of the particle, the mean stress on the particle is greater than that of the mean stress induced to the composite. This can be seen by investigating the stress transfer ratio. The average R1 PS coefficients for each size particle are shown in Table 4.5 along side the calculated hydrostatic stress ratio. The hydrostatic stress ratio is obtained by dividing the measured R1 PS coefficients by the known hydrostatic R1 PS coefficient for polycrystalline alumina, $-7.59\ cm^{-1}/GPa$ [35]. Only the R1 values are used in an effort to condense the results. The same trends are seen with both R1 and R2.

The large error for the large particle size samples is a result of including Sample 16 in the calculations. If Sample 16 is excluded from the calculations, the average R1 PS coefficient for the large particle size samples becomes $-5.498 \pm 0.221\ cm^{-1}/GPa$. Although Sample 16 could be considered an outlier and excluded from the analysis, it was included because it showed no visible anomalies.

Table 4.5: Particle size results including the R1 PS coefficient and hydrostatic stress ratio

Particle Size	R1 PS Coefficient	Hydrostatic Stress Ratio
Small	$-4.214 \pm 0.621\ cm^{-1}/GPa$	0.555 ± 0.082
Medium	$-4.558 \pm 0.133\ cm^{-1}/GPa$	0.601 ± 0.017
Large	$-4.940 \pm 1.101\ cm^{-1}/GPa$	0.651 ± 0.145

A trend is observed that as the particle size is increased the hydrostatic stress ratio increases. An increase in the hydrostatic stress ratio translates to an increase in load transfer from the matrix to the particle. This result shows that larger particles tested here provide a better environment for load transfer for the range of sizes tested. The change in particle size also resulted in a change in the matrix to particle diameter since the matrix diameter is constant. In particulate composites, the aim is to partition the load such that the particle, which provides the reinforcement, experiences larger loads. The effects of particle size for the alumina-epoxy samples tested here will be discussed in the next section.

4.1.5 Discussion

The first comparison to literature involved the overall magnitude of the PS coefficients observed here. He and Clarke measured an R1 PS coefficient of $-7.59\ cm^{-1}/GPa$ [35]

for polycrystalline alumina. Under uniaxial compression, as derived in Chapter 2, the R1 PS coefficient becomes $-2.53\ cm^{-1}/GPa$. The PS coefficients measured in this study lie within the bounds of these two values. Additionally, the effect of particle volume fraction was studied by Stevenson [61] and the measured R1 PS coefficients of $-3.19\ cm^{-1}/GPa$ and $-5.77\ cm^{-1}/GPa$ are also comparable to the values observed in this work.

With the PS coefficients validated, a comparison to Eshelby's model is made. The material properties of both the inclusion and matrix are known and can be found in Table 4.6. Using the material properties and the equations in Chapter 2, the hydrostatic stress ratio can be calculated. Eshelby's models predicts a hydrostatic stress ratio of 0.426 for a single alumina particle isolated in an infinite matrix. Results here show values as much as 58.8% higher than the value predicted by Eshelby. The infinite matrix assumption may be the cause of this because an infinite matrix would translate to an infinitesimal particle.

Table 4.6: Material Properties

Material	Modulus (GPa)	Poisson's Ratio
Alumina (Particle)	350	0.22
Epoxy (Matrix)	2.41	0.40

Lastly, overall material property comparisons are made. In literature, it has been observed that an increase in particle size causes the overall composite to become weaker.

This was quantified by measuring a reduced elastic modulus as particle size increased [44] and by observed increases in tensile strength with decreasing particle size [27]. This result is supported by the empirical model developed by Landon [42] seen in Equation 4.1, where σ_c is the strength of the composite, σ_m is the strength of the matrix, V_p in the particle volume fraction and k is the slope of the tensile strength against the mean particle size (d_p). At first glance, this is in contrast to what has been observed here because an increase in load transferred to the particle from the matrix with increased particle size should indicate a stronger material. However, these studies measured overall material properties and also investigated particle sizes ranging from 0.01 to 58 μm. As a result, the sample geometry may help explain the result.

$$\sigma_c = \sigma_m(1 - V_p) + k(d_p) \tag{4.1}$$

The increase in particle size provides a greater surface area, which supports load transfer. One study [27] made observations on polypropylene composites reinforced with spherical particles that indicated that the strength increases with increasing surface area, through a more efficient stress transfer mechanism. However, larger contact surface increases the potential for defects that result in particle to matrix bonding failure to occur. Once the particle debonds from the matrix, the particle can no longer effectively reinforce the matrix, causing the composite to fail earlier. This ultimately leads to the observation that the composite strength increases with decreasing particle size [27]. Although no trend in the overall compressive strength of the single particle composites with respect to particle size was observed, the increase in load transfer with particle size supports the theory that increased surface area facilitates load transfer.

In addition to the strength observations made in literature, increased particle size has been observed to increase fracture toughness. Many studies [43, 53] have observed increased fracture toughness with increasing particle size. An increase in load transfer in larger sized particles observed here could indicate that larger particles are able to absorb more energy during failure resulting in an increase in fracture toughness of the composite.

The effect of matrix diameter to particle diameter is not studied here, but it could be a competing factor. Additionally studies could be done in which the matrix size is varied in order to keep the matrix to particle diameter ratio constant.

4.2 Irregular Shape

In addition to the investigation of particle size, particle shape was investigated using the irregularly shaped particle samples as described in Chapter 3. The same procedure was used as in the particle size investigation to determine the R1 PS coefficients and resulting hydrostatic stress ratio. However, the data showed very sporadic behavior and only three samples provided data that could be analyzed. The unpredictable behavior is attributed to the possibility of poor bonding between the particle and matrix because of the particles irregular shape. The results are shown in Table 4.7. Again, only the R1 peak is used for the calculation of the hydrostatic stress ratio.

Table 4.7: Irregularly Shaped Particle Sample Results

Sample Number	Particle Size	R1 PS Coefficient	Hydrostatic Stress Ratio
Sample 5	$580\mu m$	$-2.577\ cm^{-1}/GPa$	$0.339\ cm^{-1}/GPa$
Sample 3	$764\mu m$	$-2.923\ cm^{-1}/GPa$	$0.385\ cm^{-1}/GPa$
Sample 8	$808\mu m$	$-7.839\ cm^{-1}/GPa$	$1.033\ cm^{-1}/GPa$

The results show that as particle size increased, so did the hydrostatic stress ratio, which indicates that although the particles are irregularly shaped, the general trend of increasing load transfer with increasing particle size is still observed. Additionally, for Sample 8, the hydrostatic stress ratio was greater than one. Multiple samples at each size were not analyzed resulting in the lack of error margins for these results. The observed value above one may fall below one if other similar samples are tested. However, this large value would indicate that the irregular shape of the particle promotes stress transfer.

This observation is in agreement with literature that observed increased wear resistance with irregularly shaped particles [9] and is also in agreement with a colleagues work which models the effect of irregular shapes using a finite element analysis [26]. Using finite element analysis it was determined that irregularly shaped particles increase the load transferred to the particle [26]. This result is supported by the fact that the irregular shape is known to cause increased stress concentrations, which increase load transfer.

4.3 Failure Mechanics Using Piezospectroscopy

The PS technique also provided interesting information on the failure of the samples. In Figure 4.10, the applied stress and measured peak shift data are both plotted versus time for one of the tested samples up to failure. It is clear that at roughly 67.5 MPa the peak position remained constant even though the load continued to be applied. This suggests that at this time, matrix yielding initiates and the particle's mean stress remains constant. This observation was made and was consistent with many of the samples that were tested to failure. Additionally, for the sample shown in Figure 4.10 the peak shift values return back to the original trend line after the plateau. This may suggest that the epoxy is failing and collapsing back onto the particle. This particle loading at failure shows a linear trend and the resulting PS coefficient is $-17.683\ cm^{-1}/GPa$. This increase from the original PS coefficient of $-5.619\ cm^{-1}/GPa$ indicates that there is a substantial increase in particle loading once the matrix begins to fail.

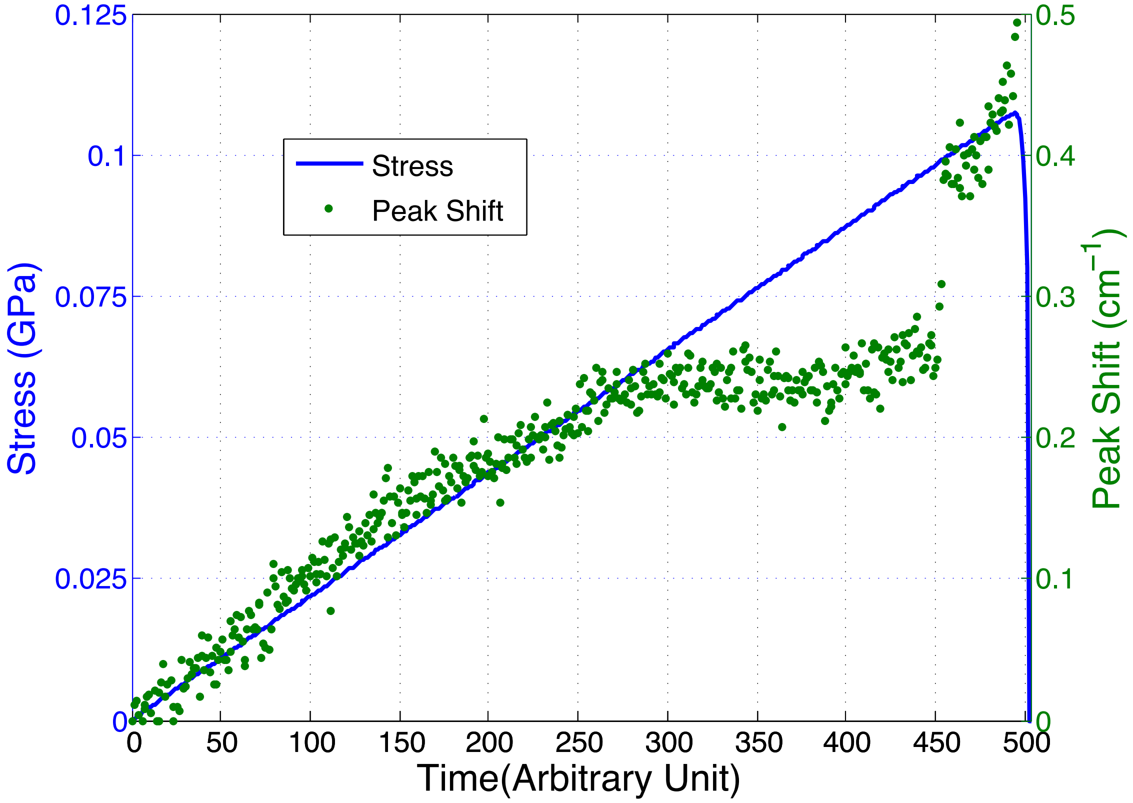

Figure 4.10: Applied uniaxial compressive stress (left) and the magnitude of the R1 peak shift (right) plotted versus time

Extensive research has been done investigating the failure of particle reinforced composites [41, 8, 10, 13] . In many cases, theoretical models, including the models discussed in previous chapters, are modified in order to gain some insight into the failure mechanics of particulate composites [36]. The topic is not investigated here but some of the interesting results are worth mentioning. Further analysis is necessary to conclusively determine the cause of the observations made in this section but many papers

[68, 27, 36, 15] point to particle-matrix interface debonding as a large contributor to failure. Since photo-stimulated luminescent spectroscopy can be used as a surface stress measurement technique, it may be a novel way to investigate the particle-matrix interface in the future. This result serves as an example of the versatility of the PS technique.

CHAPTER 5
X-RAY DIFFRACTION ANALYSIS OF ALUMINA-EPOXY SAMPLES

X-ray diffraction experiments were conducted at the Canadian Light Source in Saskatoon, Saskatchewan. The experiments were conducted at the Very Sensitive Elemental and Structural Probe Employing Radiation from a Synchrotron (VESPERS) beamline. A miniature mechanical load frame was developed at UCF specifically for use with the beamline at CLS. This chapter serves to present the results gathered from the experiments at CLS and compare them with the results gathered at UCF. The first, qualitative, analysis of the data was an observation of the diffraction pattern radius change with load. The results from the radius change investigation motivated further analysis of the data for strain using a series of analysis codes. Following the presentation of the strain results, some conclusions are drawn from the data and qualitative comparisons are made to the results from previous chapters.

5.1 Diffraction Patterns at CLS

To conserve the limited time at the beamiline, only six of the total 9 samples were tested at CLS as seen in Table 5.1. Each sample was subjected to three different compression loads and at each load, a six-point line scan was performed in the middle of the sample. The assumption of equi-biaxial strain in the transverse direction motivated the choice of the center of the particle to be used for scanning. This assumption allows for the calculation of the full stress and strain tensors. A six-point scan was chosen to have a large number of data points to average, while conserving time at the beamline. The scans were all executed at the center of the particle, from top-center (location 1) to bottom-center (location 6) as seen in Figure 5.1.

Table 5.1: List of XRD Samples

Sample Number	Matrix Diameter (mm)	Particle Diameter (mm)	Class
10	7.14	1.287 ± 0.026	Small
12	7.14	1.287 ± 0.047	Small
14	7.14	1.440 ± 0.071	Medium
15	7.14	1.420 ± 0.057	Medium
16	7.14	1.687 ± 0.046	Large
18	7.14	1.873 ± 0.036	Large

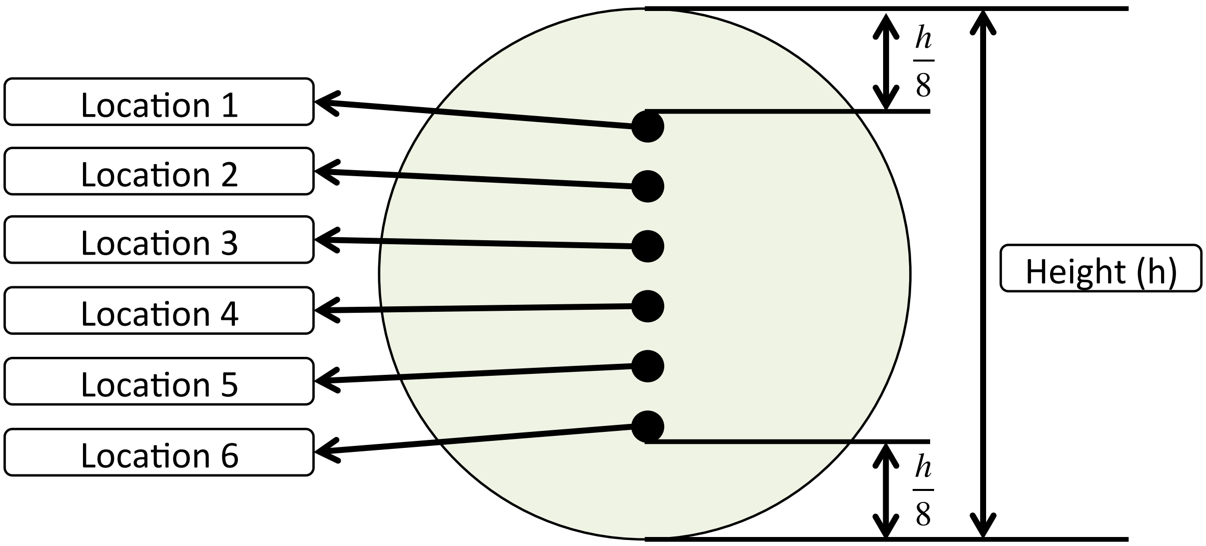

Figure 5.1: Particle scan points

The initial data collection showed show interesting characteristics that are worth pointing out. The most obvious characteristic of the diffraction patterns were the 10 different modules from the area detector at CLS as seen in Figure 5.2. There is physical space between each module that resulted in many "dead" pixels that interrupted each diffraction ring. It is clear that some rings (such as the outer rings) were affected more than others. It is also evident from Figure 5.2 that the bottom side of the diffraction pattern had some interference. This was caused by the X-Y-Z stage motor cable, which was not able to be moved. In addition to the module gaps, the beam stop holder, seen as a faint horizontal line on the left side of Figure 5.2, caused the rings to weaken in that area as well.

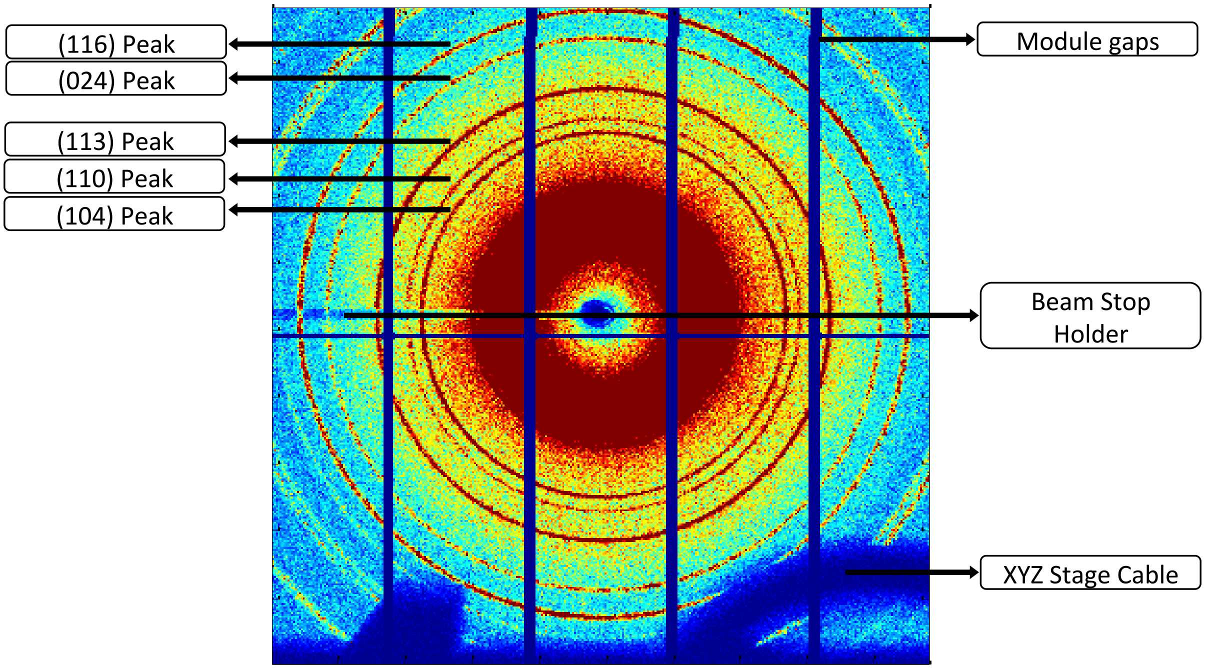

Figure 5.2: Example of a diffraction pattern collected from one of the isolated alumina particle samples

Another characteristic of the diffraction patterns was observed when investigating the location scans on the particle. At the locations away from the center of the particle, the rings appeared thicker on the bottom or top of the diffraction pattern (depending on the location of the collection). This effect can be seen in Figure 5.3, and is assumed to have been caused by the amount of material the X-rays had to penetrate. For the top of the particle, the X-ray beam had to penetrate more material on the bottom because the sphere was thicker there. As a result, the scan points that were above the middle of the particle showed thinner rings on the bottom of the raw diffraction pattern. Using the same logic, the reverse trend was observed at the scan locations below the center of the particle.

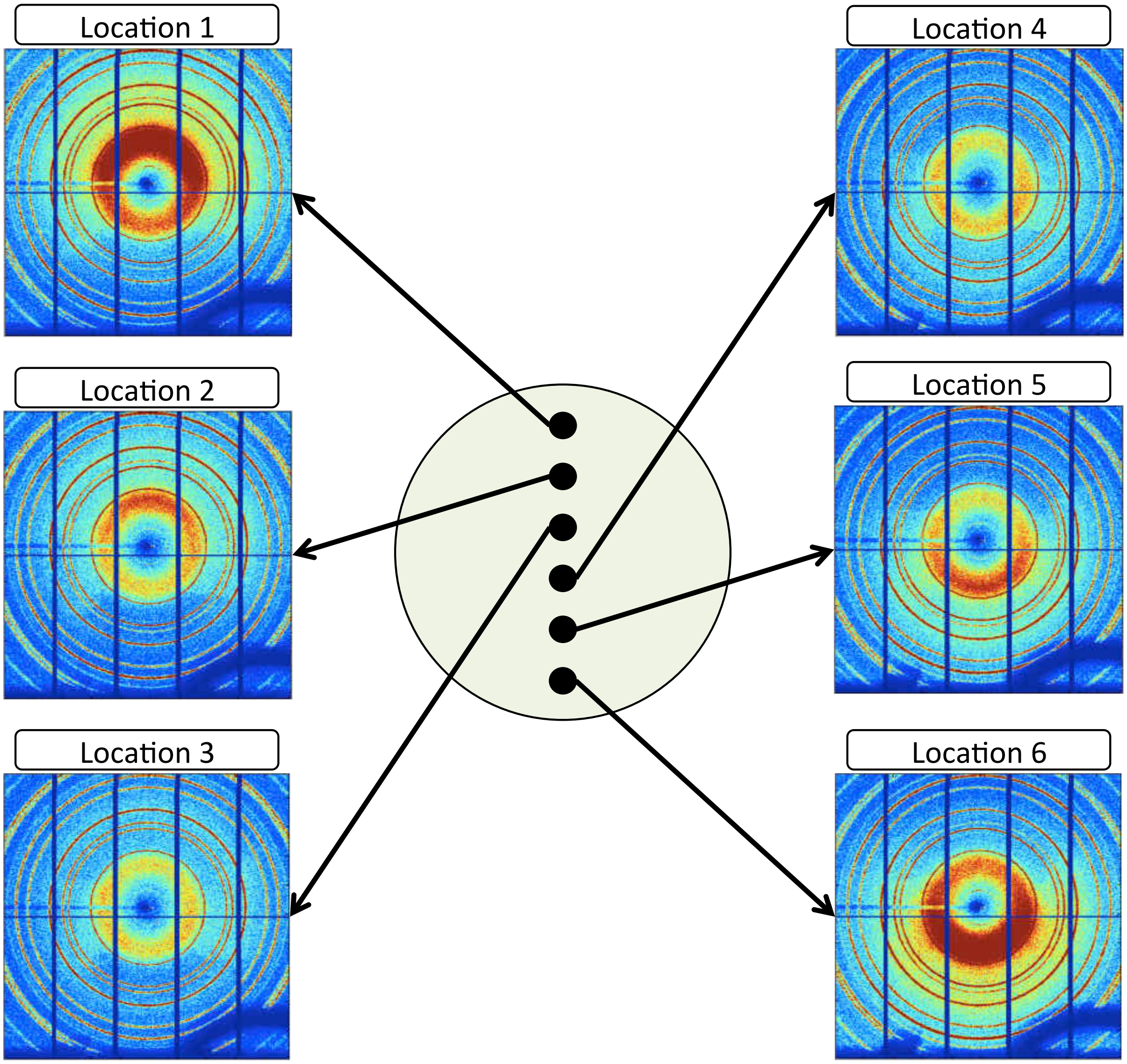

Figure 5.3: Changes in the diffraction pattern at different locations

5.2 Radius Change Results

The analysis of the data began with a qualitative look at the diffraction patterns at different loads. This was done by investigating individual points around the ring because, theoretically, each point should vary with applied load because of the increased strain on the lattice plain. This analysis of individual point radius changes proved to be extremely useful in determining the initial trends of the data. The first regions investigated were the top and bottom of the rings. In order to reduce the noise in analyzing just one point, the average radius of an azimuthal section of 7.5 degrees was used. A section of just 7.5 degrees was small enough to avoid any interference from the gaps caused by the modules. Additionally, 4 points were averaged, two at the top of the ring and two at the bottom of the ring. This averaging was done to ensure that the bias of just one section (top or bottom) of the ring was minimized. Location three was chosen for the radius change analysis to avoid any effects from the texturing of the diffraction patterns seen at other locations.

Intuitively, the radius should increase because the applied compressive load should cause the radius of the rings to grow in the vertical direction. The change in radius with applied load for the inner (104) peak was observed and the data can be seen in Tables 5.2, 5.3, and 5.4. The same analysis was done for the (113) peak and that data can be seen in Tables 5.5, 5.6, and 5.7.

Table 5.2: Small: Average radius change of the (104) peak with applied load

Sample Number	Load (N)	Average Radius (pixels)	Error (pixels)
1	0	272.50549	0.029846
	300	272.5141028	0.0483275
	600	272.4958443	0.04868
	900	272.5637689	0.039877
3	0	272.073092	0.03518275
	300	272.225528	0.027516
	600	272.248709	0.03536175
	900	272.1608058	0.0334515

Table 5.3: Medium: Average radius change of the (104) peak with applied load

Sample Number	Load (N)	Average Radius (pixels)	Error (pixels)
5	0	272.9026818	0.0188335
	300	272.8824898	0.02496175
	600	273.0040298	0.025821
	900	273.0059595	0.033907925
6	0	273.123465	0.04370725
	300	273.0098613	0.03699425
	600	273.1380808	0.02498975
	900	273.080847	0.03869725

Table 5.4: Large: Average radius change of the (104) peak with applied load

Sample Number	Load (N)	Average Radius (pixels)	Error (pixels)
7	0	272.361885	0.029557
	300	272.383171	0.037794
	600	272.4185348	0.0511155
	900	272.4971848	0.0347325
9	0	272.7371865	0.02769325
	300	272.7514958	0.03138275
	600	272.7531853	0.03402075
	900	272.7107228	0.03232225

Table 5.5: Small: Average radius change of the (113) peak with applied load

Sample Number	Load (N)	Average Radius (pixels)	Error (pixels)
1	0	338.0729475	0.03262375
	300	338.0668763	0.02714175
	600	338.0657865	0.02796075
	900	338.1124453	0.02850875
3	0	337.5130088	0.0289145
	300	337.6032825	0.03162775
	600	337.6524065	0.04133725
	900	337.6534243	0.03037175

Table 5.6: Medium: Average radius change of the (113) peak with applied load

Sample Number	Load (N)	Average Radius (pixels)	Error (pixels)
5	0	338.822825	0.0394495
	300	338.8026018	0.040641
	600	338.8605395	0.02932075
	900	338.8847253	0.03737475
6	0	338.932322	0.042575
	300	338.896989	0.0387055
	600	338.9387765	0.0371165
	900	339.0719355	0.05222125

Table 5.7: Large: Average radius change of the (113) peak with applied load

Sample Number	Load (N)	Average Radius (pixels)	Error (pixels)
7	0	337.7351195	0.03498675
	300	337.726217	0.034866
	600	337.6989968	0.03426825
	900	337.6340665	0.04087525
9	0	338.2801885	0.03817225
	300	338.2753338	0.034741
	600	338.2958445	0.037613
	900	338.2549598	0.0323385

A summary of the trends for each sample is presented in Figure 5.4 where the trend for each particle size is shown. It is clear that the (104) peak had very rough trends and it was difficult to make any conclusions from the data. However, as one moves away from the inner rings, to the (113) peak, clearer trends emerge. This notable difference in the quality of the data by using different peaks makes logical sense because the larger, outer rings will show a clearer distinction in radius change. It is observed in the (113) peak results that the small and medium sized particle samples follow a generally increasing trend. For the samples with large particles, the trend is in the opposite direction. The data for the larger particle samples seemingly shows that as compressive loads are applied, the strain in the particle is, overall, more tensile than compressive. Further investigation is necessary for confirmation of this result. On the other hand, the small and medium particle samples show that as compressive loads were applied, increasingly more compressive strains were observed in the particle. Furthermore, the maximum radius change was larger in the medium particle samples than in the small particle samples. A larger radius change translates to a larger strain. Larger strain in the comparative larger particles supports the conclusion from the PS data in Chapter 4 that as particle size increases so does load transfer.

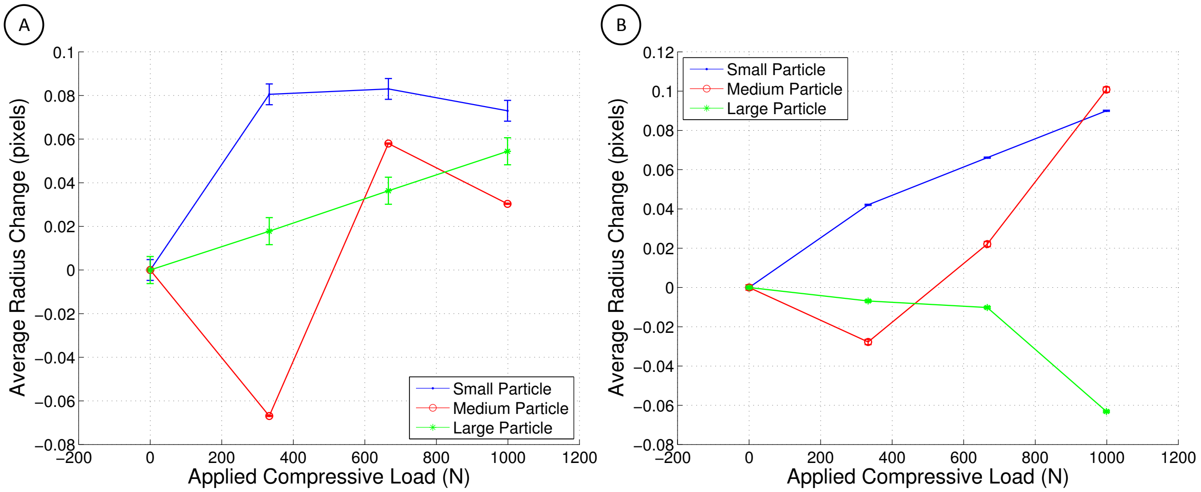

Figure 5.4: Average radius change in the (104) peak (A) and the (113) peak (B) plotted versus applied compressive load

5.3 Strain Results

The trends observed in the radius change investigation motivated further analysis of the full diffraction rings using a series of Matlab codes. The strain analysis process started by using calibration parameters that were obtained from the alumina powder sample which can be seen in Table 5.8. These were input into a set of analysis codes that were used to analyze each diffraction ring for strain. The analysis codes read in and transform the 2-D tiff file and then convert the measured radial positions to stain. As a result of the previous analysis, only the (113) peak was investigated at location 3 because it yielded clearer results. The results presented here are in terms of deviatoric strain

$(e_{22} - e_{11})$. This is done because the average change in radius of the ring is very sensitive to the placement of the sample in the mechanical loading frame. Small deviations in the placement of the sample cause the sample to detector distance to change, which causes the radius of the rings to change. This radius change results in large errors in the calculation of the hydrostatic strain.

Table 5.8: Beam, Detector and Calibration Parameters

Parameter	Value
Beam Energy	$17855eV$
Beam Size	4x4μm
Detector Size	981x1043 $pixels$
Detector Pixel Size	$172\mu m$
Sample to Detector Distance	$171.6mm$
Beam Center	$(521.46mm, 517.01mm)$
Tilt (Axis of Rotation, Rotation)	$(27.101°, 0.498°)$

The modules became more of an issue when analyzing the entire ring for strain. As seen in Figure 5.5, it is clear that the strain results for the (113) peak, without taking into account the module gaps, lead to very noisy and unpredictable trends. However, with corrections made for the modules, the trends become more pronounced. The large gaps caused by the modules were avoided by neglecting those sections of the rings when the data was fitted. A total of four regions were neglected which roughly corresponded to the top, bottom, right and left of the diffraction pattern (areas containing large gaps). By excluding these regions from the calculations the trend reversed and the magnitude of the strains increased as seen in the corrected (113) peak strain values in Figure 5.5 for Sample 12.

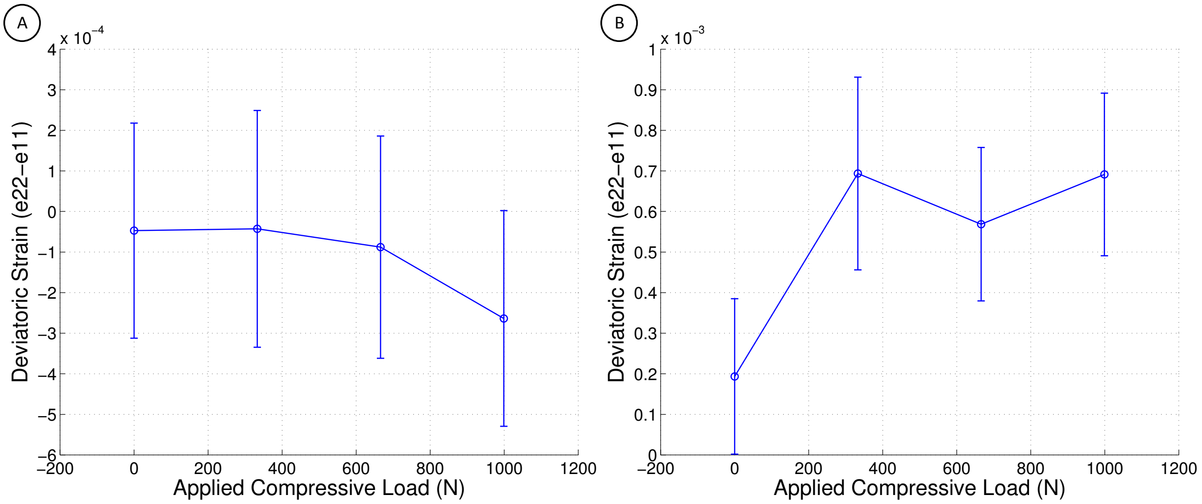

Figure 5.5: Comparison between the uncorrected (A) and corrected (B) (113) peak strains for Sample 12

With the correction in place, each of the six samples were analyzed and the results can be seen in Figures 5.6, 5.7, 5.8, 5.9, 5.10, and 5.11. For most of the samples, a rough trend of increasing deviatoric strain with applied load was observed.

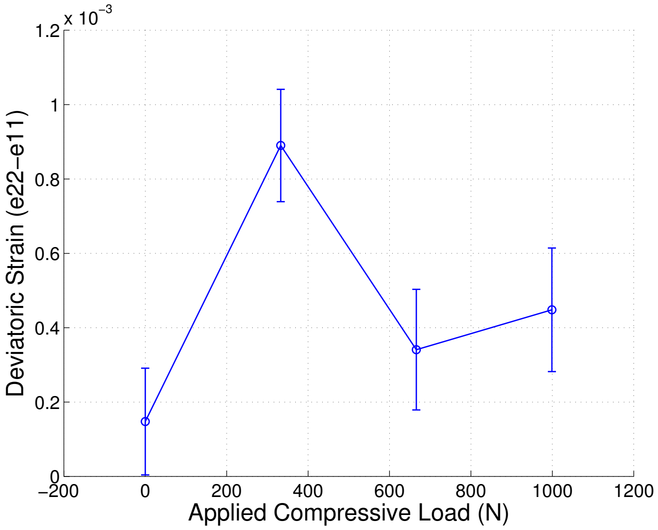

Figure 5.6: Strain from the (113) peak for Sample 10

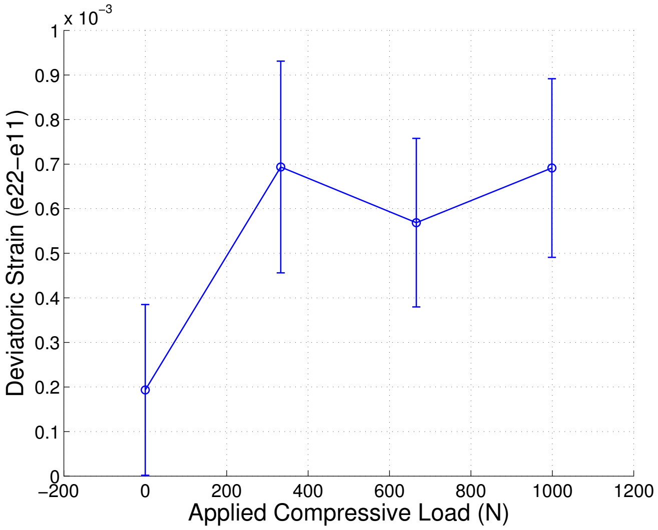

Figure 5.7: Strain from the (113) peak for Sample 12

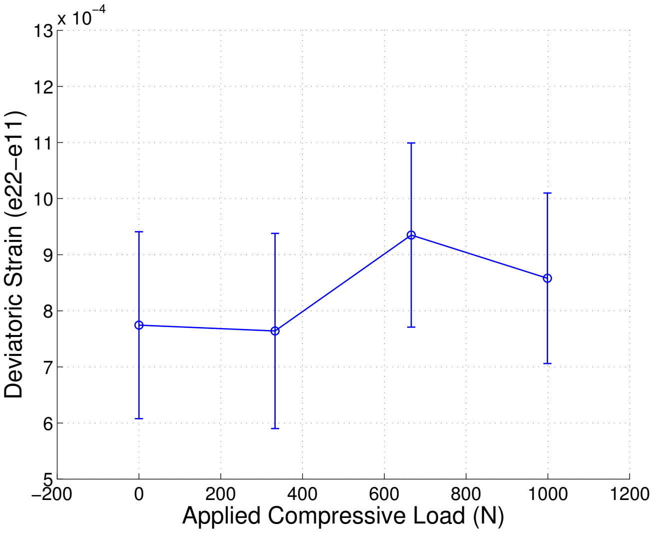

Figure 5.8: Strain from the (113) peak for Sample 14

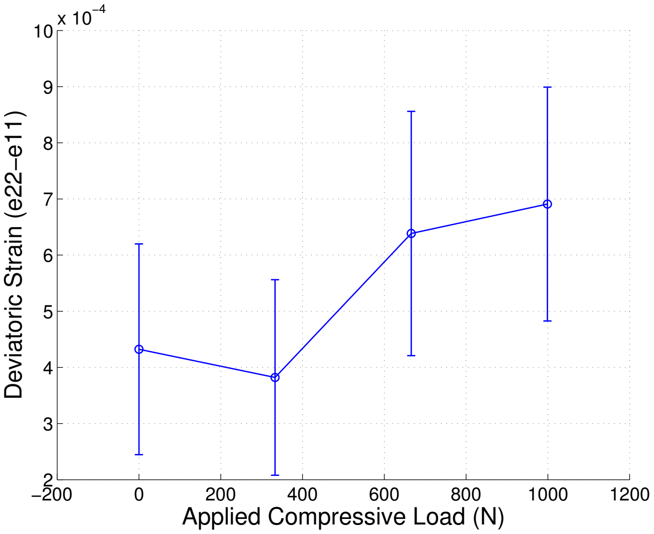

Figure 5.9: Strain from the (113) peak for Sample 15

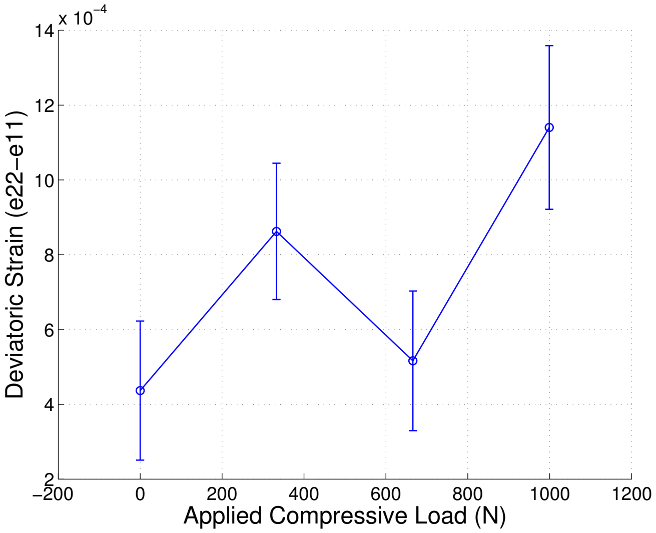

Figure 5.10: Strain from the (113) peak for Sample 16

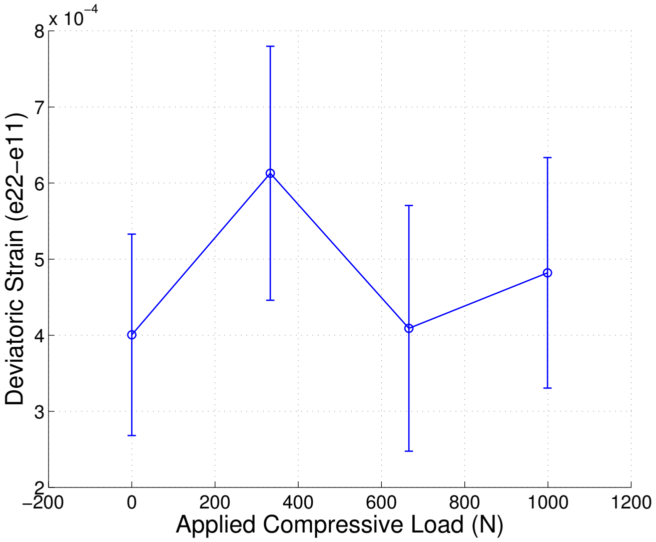

Figure 5.11: Strain from the (113) peak for Sample 18

The particle size effect on strain within the alumna particle is shown in Figure 5.12. It is observed from the plot that the larger particles experienced an increased amount of strain. Without calculating the hydrostatic strain in the particle, a quantitative comparison with the PS results in the previous chapter is not possible. However, both with PS and with XRD, increased loads on the particle were observed, as the particle size increased.

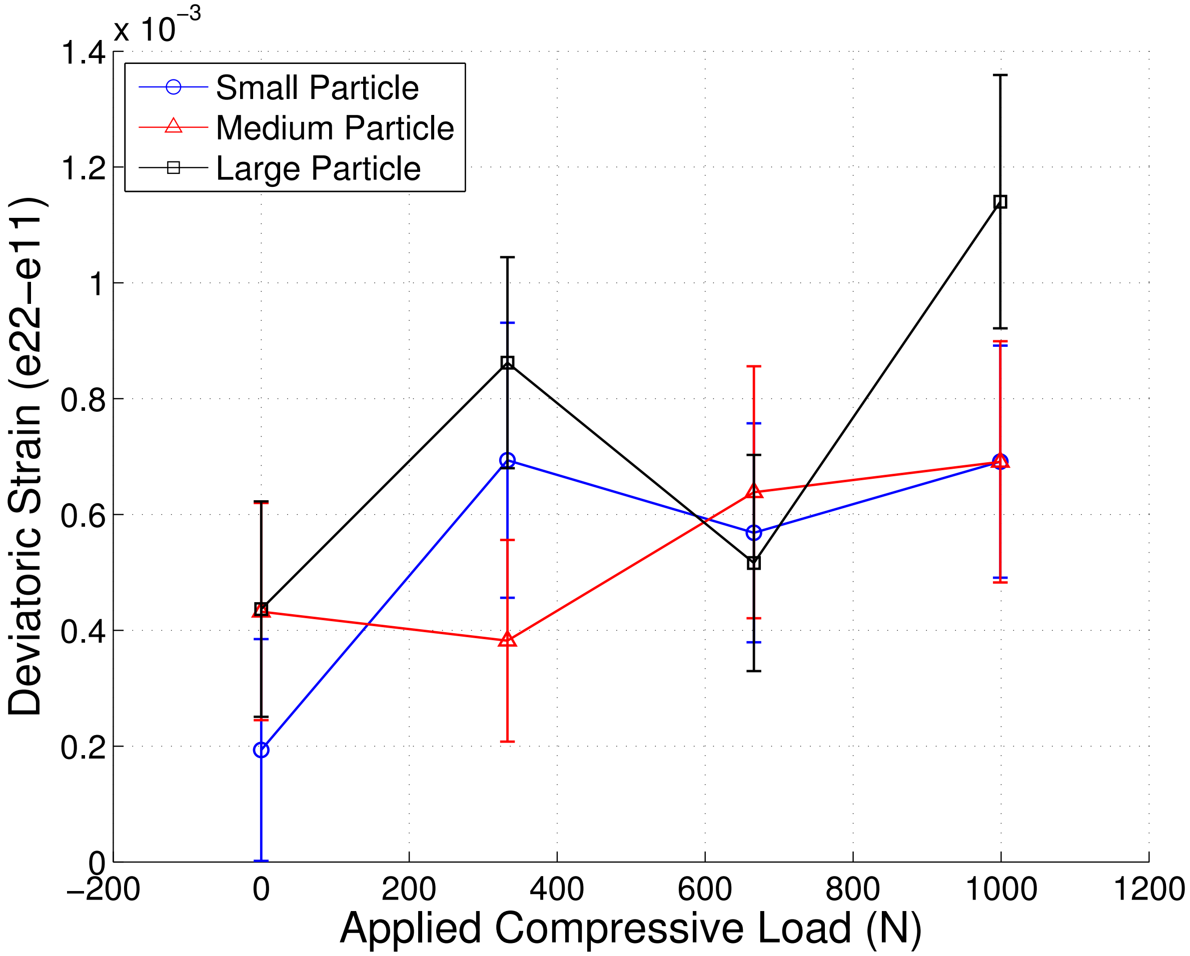

Figure 5.12: Particle size effect of strain using the (113) peak

5.4 Conclusions

Further analysis of the XRD results is necessary in order to fully understand the load transfer properties of the composite samples tested. First, the radius change and deviatoric strain results studied here must be expanded upon to include an analysis of the hydrostatic strain. As previously mentioned, because of some on the uncontrollable experimental parameters such as beam energy, large errors in the hydrostatic strain results are expected. However, the results from both studies have shown some trends that support the finding from Chapter 4. Specifically, the maximum strain in the larger particles was higher than the maximum strain in the smaller and medium sized particles. This observation supports the result of increased load transfer with increased particle size found in Chapter 4.

Additionally, another notable outcome from the XRD study is that the small loads induced in the samples caused very small changes in the XRD pattern. As a result, analysis and conclusions from the XRD data are very difficult to interpret. Comparatively, the same loads were induced in the same samples during the PS studies. With those studies, noticeable trends were observed and results were shown to correlate with literature. This XRD work, at the minimum, proves that using PS to study parameters such as particle size, shape, dispersion and volume fraction and their effect on load transfer in particulate composites is a practical method and has some advantages over XRD when investigating stiff particles such as the ceramic particles used here.

CHAPTER 6
CONCLUSIONS

The development of samples with isolated particles was achieved through a unique manufacturing method. The epoxy matrix material was partially cured in a mold that was not entirely full. This allowed for a single alumna particle to be placed in the center of the sample. The isolated spherical alumina particle samples enabled the effect of particle size on load transfer to be studied.

In-situ loading for piezospectroscopy (PS) was achieved through the use of novel instrumentation. A portable spectroscopy system was used to excite the alumina within the samples and collect the resulting spectral emission. This enabled the study of stresses on the surface and subsurface of the particle, while the matrix material was loaded in compression. In addition to the novel PS studies, in-situ X-ray diffraction (XRD) experiments were conducted. They were performed through the development of a miniature loading frame capable of applying compressive loads up to $1200N$ while XRD data was collected.

The PS results showed that increasing particle size results in increased load transfer to the particle for the sizes of particles investigated here. The PS coefficients were comparable to results from a previous study on particle volume fraction [60]. The hydrostatic stress ratios observed here were shown to be higher than the hydrostatic stress ratio predicted by the classical Eshelby model. In addition, comparisons with overall material properties from literature were made and it was concluded that an increase in surface area provides for a more efficient stress transfer mechanism. This conclusion has been seen in literature and was confirmed experimentally by the increasing hydrostatic stress ratio with increasing particle size (surface area) observed in this work. The PS results also showed experimental validation of the effect of particle shape. An observed increase in the hydrostatic stress ratio for the irregularly shaped particles studied here provides evidence that irregularly shaped particles promote load transfer from the matrix to the particle.

The XRD results showed that increased loads shifted the diffraction rings through an analysis of the change in radius of the rings. The results motivated further analysis of the data for strain using a series of Matlab codes. Once the gaps in the diffraction patterns were accounted for in the codes, the strain analysis showed increased deviatoric strain in the larger particles as compared to the medium and smaller sized particles. Although the XRD data was not as clear as the PS data, the results were in qualitative agreement. A conversion from strain to stress is necessary for quantitative validation of the PS results.

Future experiments on the effects of particle size will investigate a wider range of particle sizes. To study larger particles, an increased loading capability would be necessary at the synchrotron facility. To study smaller particles, manufacturing techniques that create nanometer sized, perfectly spherical particles would be necessary. In addition to a wider range of particles, a varying matrix size could be implemented that would account for the changing particle size in order maintain a consistent volume fraction throughout the experiments.

Overall, the results presented here show that piezospectroscopy and X-ray diffraction can be used to study parameters such as particle size and shape. The results here motivate future experiments that could investigate other reinforcing parameters such as particle dispersion, interacting particles, particle-matrix adhesion and debonding. Future experiments could be conducted with surface treated alumina to observe adhesion properties of particulate composites. Other work could investigate interacting particles by isolating multiple particles in the epoxy matrix and mapping the stress distribution in each of them. Many other experiments could be performed and the data from them could be used to validate and further refine existing load transfer theories by providing experimental measurements of the strain and stress in the particle (or particles) while loading. This critical load information is not usually measured while doing conventional mechanical testing. However, PS and XRD enable the study of these loads experimentally. Overall, these studies will help improve the design of particulate composites by providing a more complete understanding of the load transfer characteristics between the reinforcing particles and the matrix material.

LIST OF REFERENCES

[1] A. Adnan, C. Sun, and H. Mahfuz. A molecular dynamics simulation study to investigate the effect of filler size on elastic properties of polymer nanocomposites. *Composites Science and Technology*, 67(3):348–356, 2007.

[2] T. J. Ahrens. Material strength effect in the shock compression of alumina. *Journal of Applied Physics*, 39(10):4610–4616, 1968.

[3] J. Almer, G. Swift, J. Nychka, E. Ustundag, and D. Clarke. In situ synchrotron measurements of oxide growth strains. *Materials Science Forum*, 490-491:287–293, 2005.

[4] B. Ash, L. Schadler, and R. Siegel. Glass transition behavior of alumina/polymethylmethacrylate nanocomposites. *Materials Letters*, 55:83–87, 2002.

[5] B. J. Ash, D. F. Rogers, C. J. Wiegand, L. S. Schadler, R. W. Siegel, B. C. Benicewicz, and T. Apple. Mechanical properties of Al_2O_3/polymethylmethacrylate nanocomposites. *Polymer Composites*, 23:1014–1025, 2002.

[6] B. J. Ash, R. W. Siegel, and L. S. Schadler. Mechanical behavior of alumina/poly(methyl methacrylate) nanocomposites. *Macromolecules and Engineering*, 37:1358–1369, 2004.

[7] S. P. Bardakhanov, A. V. Kim, V. I. Lysenko, A. V. Nomoev, D. Y. Trufanov, M. D. Buyantuev, and D. Z. Bazarova. Properties of ceramics prepared from nanopowders. *Inorganic Materials*, 45(3):335–339, 2009.

[8] Z. P. Bazant, M. R. Tabbara, M. T. Kazemi, and G. Pijaudier-Cabot. Random particle model for fracture of aggregate or fiber composites. *Journal of Engineering Mechanics*, 116(8):1686–1705, 1990.

[9] D. L. Burris and W. G. Sawyer. Improved wear resistance in alumina-PTFE nanocomposites with irregular shaped nanoparticles. *Wear*, 260:915–918, 2006.

[10] R. Butcher, C.-E. Rousseau, and H. Tippur. A functionally graded particulate composite: preparation, measurements and failure analysis. *Acta Materialia*, 47(1):259–268, 1998.

[11] C.A.Tracy. A compression test for high strength ceramics. *Journal of Testing and Evaluation*, 15:14–19, 1987.

[12] Chang and Yeih. The effects of particle shape on bond strength improvement of epoxy-particle coating composites. *Journal of Marine Science and Technology*, 9(2):153–160, 2001.

[13] B. Chiaia, A. Vervuurt, and J. Van Mier. Lattice model evaluation of progressive failure in disordered particle composites. *Engineering Fracture Mechanics*, 57(2):301–318, 1997.

[14] N. Chisholm, H. Mahfuz, V. K. Rangari, A. Ashfaq, and S. Jeelani. Fabrication and mechanical characterization of carbon/SiC-epoxy nanocomposites. *Composite Structures*, 67:115–124, 2005.

[15] J. Cho, M. Joshi, and C. Sun. Effect of inclusion size on mechanical properties of polymeric composites with micro and nano particles. *Composites Science and Technology*, 66:1941–1952, 2006.

[16] J. Colby A. Foss, G. L. Hornyak, J. A. Stockert, , and C. R. Martin. Template-synthesized nanoscopic gold particles: Optical spectra and the effects of particle size and shape. *The Journal of Physical Chemistry*, 98:2963–2971, 1994.

[17] V. Corral-Flores, D. Bueno-Baques, D. Carrillo-Flores, and J. Matutes-Aquino. Enhanced magnetoelectric effect in core-shell particulate composites. *Journal of Applied Physics*, 99(8):08J503, 2006.

[18] C. Dancer, H. Curtis, S. Bennett, N. Petrinic, and R. Todd. High strain rate indentation-induced deformation in alumina ceramics measured by Cr^{3+} fluorescence mapping. *Journal of the European Ceramic Society*, 31:2177–2187, 2011.

[19] B. Derby. Ceramic nanocomposites: mechanical properties. *Current Opinion in Solid State and Materials Science*, 3:490–495, 1998.

[20] R. O. Diaz. In-situ stress measurements of eb-pvd thermal barrier coatings using synchrotron x-ray diffraction under thermo-mechanical loading. Master's thesis, University of Central Florida, 2010.

[21] J. Durand, M. Vardavoulias, and M. Jeandin. Role of reinforcing ceramic particles in the wear behaviour of polymer-based model composites. *Wear*, 181:833–839, 1995.

[22] E. Durnberg, I. Hanhan, G. Freihofer, and S. Raghavan. Experimental piezospectroscopic measurements to study load transfer in a single alumina particle embedded within an epoxy matrix. In *proceedings of the Society for the Advancement of Material and Process Engineering Conference*, 2014.

[23] L. C. Erickson, T. Troczynski, H. M. Hawthorne, H. Tai, and D. Ross. Alumina coatings by plasma spraying of monosize sapphire particles. *Journal of Thermal Spray Technology*, 8:421–426, 1999.

[24] J. D. Eshelby. The determmination of the elastic field of an ellipsoidal inclusion and related problems. *Proceedings of the Royal Society of London. Series A, Mathematical and Physical Sciences*, 241:376–396, 1957.

[25] G. Freihofer, S. Frank, E. Ergin, A. Jones, A. Stevenson, A. Schlzgen, H. Tat, and S. Raghavan. Measurement of load transfer within alumina nanoparticle epoxy composites using piezospectroscopy. In *proceedings of the Society for the Advancement of Material and Process Engineering Conference*, 2013.

[26] G. J. Freihofer. *Nanocomposite Coating Mechanics via Piezospectroscopy.* PhD thesis, University of Central Florida, 2014.

[27] S.-Y. Fu, X.-Q. Feng, B. Lauke, and Y.-W. Mai. Effects of particle size, particle/matrix interface adhesion and particle loading on mechanical properties of particulate–polymer composites. *Composites Part B: Engineering*, 39(6):933–961, 2008.

[28] E. N. Gilbert, B. S. Hayes, and J. C. Seferis. Nano-alumina modified epoxy based film adhesives. *Polymer Engineering and Science*, 43:1096–1104, May 2003.

[29] L. Grabner. Spectroscopic technique for the measurement of residual stress in sintered Al_2O_3. *Journal of Applied Physics*, 49(5):580–583, 1978.

[30] Z. Guo, T. Pereira, O. Choi, Y. Wang, and H. T. Hahn. Surface functionalized alumina nanoparticle filled polymeric nanocomposites with enhanced mechanical properties. *Journal of Materials Chemistry*, 16:2800–2808, 2006.

[31] A. P. Hammersley. European Synchrotron Research Facility (ESRF), internal report. ESRF98HA01T, FIT2D V9.129 reference manual V3.1. Technical report, ESRF, Grenoble, France, 1998.

[32] Harding, Page, Manson, and Berg. Measurement of residual stress effects by means of single-particle composite tests. *Journal of Adhesion Science and Technology*, 12(5):497–506, 1998.

[33] P. Harding and J. Berg. The characterization of interfacial strength using single-particle composites. *Journal of adhesion science and technology*, 11(8):1063–1076, 1997.

[34] B. He. Introduction to two-dimensional X-ray diffraction. *Powder Diffraction*, 18(2):71–85, June 2003.

[35] J. He and D. R. Clarke. Determination of the piezospectroscopic coefficients for chromium doped sapphire. *Journal of American Ceramic Society*, 78(5):1347–1353, 1995.

[36] H. M. Inglis. *Modeling the effect of debonding on the constitutive response of heterogeneous materials.* PhD thesis, University of Illinois at Urbana-Champaign, 2014.

[37] P. K. Jain, K. S. Lee, I. H. El-Sayed, and M. A. El-Sayed. Calculated absorption and scattering properties of gold nanoparticles of different size, shape, and composition: Applications in biological imaging and biomedicine. *The Journal of Physical Chemistry B*, 110:7238–7248, 2006.

[38] R. Jenkins and R. Snyder. *Introduction to X-ray powder diffractometry*, volume 267. John Wiley & Sons, 2012.

[39] D. Jordan and K. Faber. X-ray residual stress analysis of a ceramic thermal barrier coating undergoing thermal cycling. *Thin Solid Films*, 235(1):137–141, 1993.

[40] J. L. Jordan, L. Ferranti, R. A. Austin, R. D. Dick, J. R. Foley, N. N. Thadhani, D. L. McDowell, and D. J. Benson. Equation of state of aluminum-iron oxide-epoxy composite. *Journal of Applied Physics*, 101(093520):1–9, 2007.

[41] A. Kinloch, D. Maxwell, and R. Young. The fracture of hybrid-particulate composites. *Journal of Materials Science*, 20(11):4169–4184, 1985.

[42] G. Landon, G. Lewis, and G. Boden. The influence of particle size on the tensile strength of particulatefilled polymers. *Journal of Materials Science*, 12(8):1605–1613, 1977.

[43] F. Lange and K. Radford. Fracture energy of an epoxy composite system. *Journal of Materials Science*, 6(9):1197–1203, 1971.

[44] B. Lauke. On the effect of particle size on fracture toughness of polymer composites. *Composites Science and Technology*, 68(15):3365–3372, 2008.

[45] G.-W. Lee, M. Park, J. Kim, J. I. Lee, and H. G. Yoon. Enhanced thermal conductivity of polymer composites filled with hybrid filler. *Composites Part A: Applied Science and Manufacturing*, 37(5):727–734, 2006.

[46] D. M. Lipkin and D. R. Clarke. Measurement of the stress in oxide scales formed by oxidation of alumina-forming alloys. *Oxidation of Metals*, 45(3):267–280, 1996.

[47] X. Liu and G. Hu. A continuum micromechanical theory of overall plasticity for particulate composites including particle size effect. *International journal of plasticity*, 21(4):777–799, 2005.

[48] P. R. Marur, R. C. Batrab, G. Garcia, and A. C. Loos. Static and dynamic fracture toughness of epoxy/alumina composite with submicron inclusions. *Journal of Materials Science*, 39:1437–1440, 2004.

[49] T. Mori and K. Tanaka. Average stress in matrix and average elastic energy of materials with misfitting inclusions. *Acta metallurgica*, 21(5):571–574, 1973.

[50] T. Mura. *Micromechanics of defects in solids*, volume 3. Springer, 1987.

[51] C. Ng, L. Scbadler, and R. Siegel. Synthesis and mechanical properties of TiO_2-epoxy nanocomposites. *NanoStructured Materials*, 12:507–510, 1999.

[52] G. Odegard, T. Clancy, and T. Gates. Modeling of the mechanical properties of nanoparticle/polymer composites. *Polymer*, 46(2):553–562, 2005.

[53] K. Radford. The mechanical properties of an epoxy resin with a second phase dispersion. *Journal of Materials Science*, 6(10):1286–1291, 1971.

[54] S. Raghavan and P. Imbrie. High-resolution stress mapping of polycrytalline alumina compression using synchrotron x-ray diffraction. *Synchrotron Radiation*, 18:497–505, 2011.

[55] R. M. Rodgers, H. Mahfuz, V. K. Rangari, N. Chisholm, and S. Jeelani. Infusion of SiC nanoparticles into sc-15 epoxy: An investigation of thermal and mechanical response. *Macromolecular Materials and Engineering*, 290:423429, 2005.

[56] D. K. Shukla and V. Parameswaran. Epoxy composites with 200 nm thick alumina platelets as reinforcements. *Journal of Material Science*, 42:5964–5972, 2007.

[57] J. S. Smith, D. Bedrov, and G. D. Smith. A molecular dynamics simulation study of nanoparticle interactions in a model polymer-nanoparticle composite. *Composites science and technology*, 63(11):1599–1605, 2003.

[58] B. Sobhani Aragh, A. Nasrollah Barati, and H. Hedayati. Eshelby–mori–tanaka approach for vibrational behavior of continuously graded carbon nanotube-reinforced cylindrical panels. *Composites Part B: Engineering*, 43(4):1943–1954, 2012.

[59] A. Steuwer, J. R. Santisteban, M. Turski, P. J. Withers, and T. Buslaps. High-resolution strain mapping in bulk samples using full-profile analysis of energy-dispersive synchrotron x-ray diffraction data. *Journal of Applied Crystallography*, 37:883–889, 2005.

[60] A. Stevenson, A. Jones, and S. Raghavan. Characterization of particle dispersion and volume fraction in alumina-filled epoxy nanocomposites using photo-stimulated luminescence spectroscopy. *Polymer*, 43:17, 2011.

[61] A. Stevenson, A. Jones, and S. Raghavan. Stress-sensing nanomaterial calibrated with photostimulated luminescence emission. *Nano Letters*, 11:3274–3278, 2011.

[62] H. Tan, Y. Huang, C. Liu, and P. Geubelle. The mori–tanaka method for composite materials with nonlinear interface debonding. *International Journal of Plasticity*, 21(10):1890–1918, 2005.

[63] J. C. Thesken and B. Lerch. Particulate titanium matrix composites tested-show promise for space propulsion applications. 2003.

[64] W.-H. Tuan and Y.-P. Pai. Mechanical properties of $Al_2O_3 - NiAl$ composites. *Journal of American Ceramic Society*, 82:1624–1626, 1999.

[65] B. Wetzel, P. Rosso, F. Haupert, and K. Friedrich. Epoxy nanocomposites - fracture and toughening mechanisms. *Engineering Fracture Mechanics*, 73:2375–2398, 2006.

[66] M. H. Wichmann, J. Sumfleth, F. H. Gojny, M. Quaresimin, B. Fiedler, and K. Schulte. Glass-fibre-reinforced composites with enhanced mechanical and electrical properties–benefits and limitations of a nanoparticle modified matrix. *Engineering Fracture Mechanics*, 73(16):2346–2359, 2006.

[67] Z. H. Xu and D. Rowcliffe. Nanoindentation on diamond-like carbon and alumina coatings. *Surface and Coatings Technology*, 161:44–51, 2002.

[68] S. C. Zunjarrao and R. P. Singh. Characterization of the fracture behavior of epoxy reinforced with nanometer and micrometer sized aluminum particles. *Composites Science and Technology*, 66:2296–2305, 2006.